

First results from SAM-FP: Fabry-Perot observations with ground layer adaptive optics – The structure and kinematics of the core of 30 Doradus

C. Mendes de Oliveira,¹★ P. Amram,² Bruno C. Quint,³ S. Torres-Flores,⁴

R. Barbá⁴ and D. Andrade¹

¹ Instituto de Astronomia, Geofísica e Ciências Atmosféricas da Universidade de São Paulo, Cidade Universitária, CEP:05508-900, São Paulo, SP, Brazil

² Aix Marseille Université, CNRS, LAM (Laboratoire d'Astrophysique de Marseille) UMR 7326, 13388, Marseille, France

³ Cerro Tololo Inter-American Observatory, SOAR Telescope, Casilla 603, La Serena, Chile

⁴ Departamento de Física y Astronomía, Universidad de La Serena, Av. Cisternas 1200, La Serena, Chile

Accepted XXX. Received YYY; in original form ZZZ

ABSTRACT

The aim of this paper is to present the first data set obtained with SAM-FP, a Fabry-Perot mounted inside the SOAR telescope Adaptive-Optics Module. This is the only imaging Fabry-Perot interferometer using laser-assisted ground layer adaptive optics, over a 3×3 arcmin² field of view. SAM-FP was used to observe the ionized gas, traced by H α , in the center of the 30 Doradus starburst (the Tarantula Nebula) in the LMC, with high spatial (~ 0.6 arcsec, or 0.15 pc) and spectral ($R \approx 11200$) resolution. Radial velocity, velocity dispersion and monochromatic maps were derived. The region displays a mix of narrow, $\sigma \sim 20$ km s⁻¹ profiles and multiple broader profiles with $\sigma \sim 70$ - 80 km s⁻¹, indicating the complex nature of the nebula kinematics. A preliminary analysis of the observations reveals the following results: i) a new expanding bubble with a projected $r=5.6$ pc radius and an expansion velocity of 29 km/s is found; ii) the Eastern filamentary loop is redshifted by $\sim 37 \pm 13$ km s⁻¹ with respect to the Northeastern filament, indicating that these complexes are two kinematically independent structures; iii) there is a clear velocity gradient in the Northeastern filament, with increasingly more negative velocities running from West to Northeast; iv) small-scale high-velocity clouds are seen throughout the “Christmas tree” cavity, probably a result of the interplay between the overall complex gas kinematics with the clumpy environment of the nebula. These data exemplify the power of the combination of a high-order Fabry-Perot with wide-field GLAO for high-resolution spatial and spectral studies. In particular, SAM-FP data cubes present great advantage over other multi-fiber or long-slit data sets in the search for small-scale bubbles in nebulae.

Key words: Instrumentation: high angular resolution, spectrographs – ISM: bubbles, kinematics and dynamics, HII regions – (galaxies:) Magellanic Clouds

1 INTRODUCTION

This paper introduces a new restricted-use instrument¹ for the SOAR telescope, or more precisely, it describes a new mode in-

side an existing facility instrument. It consists of a Fabry-Perot device mounted inside the SOAR Adaptive Module (SAM) with the SAM imager (SAMI, the existing imager regularly used with SAM), to deliver high spatial resolution data cubes, with high and low spectral resolutions, in the optical, with a field of view of 3×3 arcmin². This new mode is hereafter referred to as SAM-FP. There are two Fabry-Perot instruments available for use with SAM-FP, a high resolution, ($R \approx 11200$ at H α) and a low resolution (tunable filter, $R \approx 4087$ at H α).

In Mendes de Oliveira et al. (2013) a number of recent Fabry-Perot spectrometers available for astronomy were described, but all of them were seeing-limited with a spatial sampling that depended

★ E-mail: claudia.oliveira@iag.usp.br

¹ Restricted-use instruments at SOAR (Southern Astrophysical Research Telescope, a 4.1-meter aperture telescope located on Cerro Pachón, Chile) are those brought to the telescope and owned and maintained by individual scientists and/or their research groups. Scientists outside the team are welcome to use this mode and, if interested, should contact one of the first three authors.

on the detector pixel scale. Here, we highlight the potential for various studies, of the SAM-FP instrument, with a pixel size of 0.045 arcsec/pixel and ground layer adaptive optics (GLAO) correction down to 0.3". A high-order Fabry-Perot with GLAO can be a unique tool in the study of kinematics of emission-line objects such as star forming galaxies, gas flows, planetary nebulae, HH objects, giant HII regions, among others. A tunable filter with GLAO, on the other hand, can be used for studying AGNs and QSOs, outflows, massive young stars, mass loss processes and Ly α detection studies, to give a few examples. In this paper we focus on data taken with the high-order, high-resolution Fabry-Perot device.

We present Fabry-Perot data cubes for the large-diameter expanding structures around a giant HII region, the center of 30 Doradus starburst (or 30 Doradus giant star forming region) also called the Tarantula Nebula, in the Large Magellanic Cloud. The study of shells and bubbles, due to stellar winds and supernova explosions, within giant HII regions is crucial for understanding the processes of mass and energy transfer from the stellar component to the interstellar medium and the processes of triggering of star formation. Although kinematic studies of super-giant shells and super-bubbles in giant HII regions are common in the literature, carried out both with long slit and more recently with 3D spectroscopy, they have not had the necessary coverage and spatial resolution to answer a few key questions. Even the origin of the supersonic motions present in these regions is still a matter of debate (Melnick et al. 1999). Moreover, it is still not understood if the kinematics of giant HII regions are due to an underlying diffuse component or to superposed multiple kinematic components. Having high spatial and spectral resolution velocity maps, as those delivered by SAM-FP, is crucial to tackle these problems.

A few authors have studied the kinematics of the ionized gas in the 30 Dor nebula, e.g. Chu & Kennicutt (1994), Melnick et al. (1999), Redman et al. (2003), Torres-Flores et al. (2013) and references therein. All of these studies reported broad and possibly multiple components widespread in the nebula, which indicates a complex structure. These studies were either performed (i) with long-slit echelle spectroscopy (e.g. Chu and Kennicutt 1994; Melnick et al. 1999), probing motions and physical conditions in small (pc) and larger (tens of pcs) scales but covering only a limited number of lines of sight or (ii) with fibers, as the work of Torres-Flores et al. (2013), with a somewhat larger field of view, but probing the nebula in a sparse manner (every 5x5 pc², with a filling factor of 0.0028). The advantage of the present study is that it combines 3D spectroscopy information with *continuous* coverage of the field over a fairly large field of view, with a pixel size of 0.18 arcsec (0.045 pc). These data show that the kinematic profiles change on scales of a tenth of a parsec over the whole field. The wealth of details seen in Hubble Space Telescope (HST) images of nearby giant HII regions can now be investigated using similar quality kinematic data taken with SAM-FP with a laser guide star.

The main purpose of this paper is to highlight the potential of Fabry-Perot maps obtained with adaptive optics in the study of 30 Dor and similar giant HII regions. The high-resolution Fabry-Perot was used to observe the ionized gas within 30 Dor, in its strongest optical line: H α . In section 2, we first describe the new mode of SAM with a Fabry Perot, SAM-FP. We also include in this section a general description of the data reduction. The observations are presented in section 3. Section 4 compares the present observations with earlier ones taken with a different instrument. We finally describe in section 5 our results which include monochromatic, radial velocity, velocity dispersion and channel maps of the region. We identify a new expanding bubble in the center of 30 Dor

and we describe the overall kinematic features observed, thanks to the high spatial resolution and continuous spatial coverage of the data. Section 6 summarizes our main results. Appendix A details all steps necessary for taking Fabry-Perot observations with SAM-FP. Appendix B provides further information on section 2.2 and Appendix A. At the adopted distance of 50 kpc to 30 Dor, 4 arcsecs corresponds to 1 pc.

A detailed kinematic study of the system is outside the scope of this work and is deferred to a future paper.

2 DESCRIPTION OF THE INSTRUMENT

2.1 SAM-FP: a new mode for SAM

The SAM instrument (Tokovinin et al. 2008) is a unique facility instrument mounted on the 4.1m SOAR telescope at Cerro Pachón. SAM improves image quality by partial correction of turbulence near the ground using ground-layer adaptive optics (Tokovinin et al. 2010, Tokovinin et al. 2012). This instrument can feed corrected images either to a visitor instrument or to the internal wide-field optical imager, SAMI (Fraga et al. 2013). SAMI works with a single e2v CCD with 4096 \times 4112 pixel². Each pixel is 15 μ m square, the pixel scale is 45.4 mas and the total field of view is 3 \times 3 arcmin². The CCD is operated with the SDSU-III controller, which reads the full unbinned chip in 10 seconds with a noise of 3.8 electrons (without patterns) and a gain of 2.1 electrons/ADU. SAM can provide very sharp images with image quality as good as \sim 0.3 arcsec in the r-band, in favorable conditions, after laser corrections. SAMI is regularly mounted on SAM for use of the SOAR community and has been used with success (e.g. Fraga et al. 2013).

SAM was built with space in the collimated beam for the installation of an etalon, to enable future Fabry-Perot observations, which had not been implemented until now. There are two Fabry-Perot instruments available for use with SAM, a high ($R \simeq 11200$) and a low ($R \sim 4087$) resolution one.

In a test run, the high-resolution Fabry-Perot, having a pupil of 65mm (ICOS ET-65²), was mounted in SAM. It has a mean gap of 200 μ m and, at H α 6563 Å, an interference order $p \simeq 609$, a finesse $F \simeq 18.5$ and $R \simeq 11200$. It has a broadband coating covering the range 400-700 nm with a reflectivity of 90%. This coating was inspected in 2015 by ICOS and was found to be in good condition. We present details about the observations described in this paper, carried out with this Fabry-Perot device, in Table 1.

The second Fabry-Perot, the low-resolution one, with a pupil size of 70mm (ICOS ET-70³), has not yet been tested in SAM, but results in the lab show it is also ready for use. It has a gap of 46 μ m and an interference order of $p \simeq 134$, a finesse $F \simeq 30.5$ and $R \simeq 4087$ at H α 6563 Å.

Both etalons are controlled by a CS100 controller (Serial Number 8030), borrowed from the Anglo Australian Observatory. The CS100 controller is linked to the Fabry Perot by a cable provided by ICOS. The controller sits in a specifically built mechanical adaptor which is fixed to the instrument support structure in a position

² This was fabricated in 1988 by Queensgate, nowadays called IC optical Systems (ICOS), for the Anglo Australian Observatory and it is, presently, in an extended loan to the University of São Paulo, kindly made possible by the present director Dr. Warrick Couch and the previous director Dr. Matthews Colless.

³ This was fabricated by Queensgate for the University of Maryland and was kindly loaned by Dr. Sylvain Veilleux.

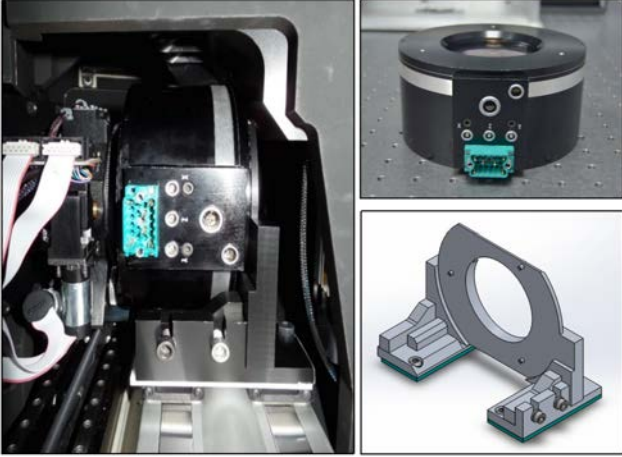


Figure 1. Upper right: photo of the high-resolution Fabry-Perot after the handles were removed. The etalon has the following dimensions: a diameter of 150 mm and a height of 76.61 mm. Lower right: 3D model of the mechanical adaptor of the Fabry Perot with pins for support in the back side; it accommodates both the low-resolution and the high-resolution Fabry-Perot devices. Left: photo of the Fabry-Perot and adaptor mounted inside SAM. Note that the Fabry-Perot fits very tightly in the space available, with ~ 1 mm clearance on either side.

that allows access to it while simultaneously inspecting the etalon. The computer that runs the CS100 is located on one side of the Nasmyth platform where SAM is permanently mounted. The CS100 contains two channels, X and Y, to control the parallelism between the Fabry-Perot plates, and a Z channel to control the spacing. A similar CS100 to the one used here is described in detail by Veilleux et al. (2010).

SAM's original concept already included a mechanism to put the Fabry-Perot in and out of the beam, which can now be used when doing Fabry-Perot observations. In order to be installed in the instrument, the mechanical housing of the Fabry-Perot ICOS ET-65 had to be cut in its diameter (performed at ICOS - the excised parts were two "ears", or handles, which were previously where the gray stripe is seen in an otherwise black Fabry-Perot body - See Figure 1). Without this change the high-resolution Fabry-Perot would not have fit inside the tight SAM space allocated for it. The low-resolution Fabry-Perot (ICOS ET-70) does not present the handle and it has the right size to be installed in the instrument. In addition, a mechanical plate adaptor needed to be fabricated in order to mount either of the two available Fabry-Perot devices inside SAM. This adaptor can be removed at any time but it is now regularly placed into SAM. It was devised in a way to allow the Fabry-Perot to be easily placed in and out of the instrument, facilitating the task of checking the parallelism while tuning the CS100, which is located immediately beside it. A picture of the high-resolution Fabry-Perot, after its handles were removed, the 3D model of the adaptor devised to house the Fabry-Perot in the instrument and a picture of the high-resolution Fabry-Perot mounted in its mechanical plate adaptor, in SAM are shown in Figure 1.

2.2 Data Acquisition

The existing control software of SAMI was modified (from a module previously written for the Brazilian Tunable Filter Imager, Mendes de Oliveira et al. 2013) in order to create a script for taking a scanning sequence. The script was used during the setup of the

Fabry-Perot, for on-sky observations, as well as for acquisition of spectral calibrations. The reasons for each command and descriptions of how the Fabry-Perot parameters are actually determined are described in the appendices. In summary, the script allows computing the exact value for the free spectral range of the Fabry-Perot device, finds the ideal number of steps needed to scan the free spectral range and defines a scanning sequence. Depending on the science case, different Fabry-Perot devices may be selected. As for a grism, the wavelength range and the spectral resolution are the important parameters when choosing the most suitable Fabry-Perot device. However, for a Fabry-Perot, the effective spectral range is in fact the free spectral range (FSR), see relation (2) below, and the spectral resolution depends on the interference order p and the finesse F , which follows relation (4) below.

2.2.1 Determining the free spectral range, the finesse and spectral resolution

In order to compute the FSR at a given wavelength λ , the interference order p should be known and it is linked to the other quantities by the basic Fabry-Perot relation:

$$p = \frac{2ne \cos \theta}{\lambda} \quad (1)$$

where $n(T = 0^\circ C, P = 1 \text{ atm}) \simeq 1.0003$ is the index of the air layer between the plates of the Fabry-Perot device, e the inner separation between the coated plates, θ the incidence angle and λ the wavelength. From equation (1), it follows that for a given n , e and θ , the FSR at the interference order p and at the wavelength λ can be computed by:

$$\Delta \lambda_{FSR} = \frac{\lambda}{p} \left(\frac{1}{1 - \frac{1}{p^2}} \right) \quad (2)$$

Conversely, for a given n , λ and θ , again from equation (1), the FSR at the interference order p and at the inner separation of the plates e can be computed by:

$$\Delta e_{FSR} = \frac{e}{p} = \frac{\lambda}{2n \cos \theta} \quad (3)$$

$\Delta \lambda_{FSR}$ is then the FSR in \AA (if λ is given in \AA), which can be easily related to the FSR in velocity units (see numerical values below), while e_{FSR} is the increment of plate separation necessary to scan the FSR.

As described in the previous sections, two Fabry-Perot devices are presently available, ICOS ET-65 having a high interference order $p \simeq 609$, at $H\alpha$, allowing coverage over a $FSR \simeq 10.8 \text{\AA}$ (following equation 2), which corresponds to $\simeq 492 \text{ km s}^{-1}$ and ICOS ET-70, with a lower interference order, $p \simeq 134$ at $H\alpha$, providing a $FSR \simeq 49.0 \text{\AA}$, which in velocity corresponds to $\simeq 2237 \text{ km s}^{-1}$.

In order to select only one or a few interference orders, an interference filter selecting a passband broader than the FSR has to be placed in the optical path, generally at (or close to) the focal plane to avoid wavelength dependence. Ideally the central wavelength of the interference filter should correspond to the mean velocity of the source. For instance, for the observations of 30 Dor with a velocity resframe of $V_s = 267 \text{ km s}^{-1}$ (Torres-Flores et al. 2013, placing $H\alpha$ at $\lambda = 6568.65 \text{\AA}$), we selected an interference filter centered at $\lambda_c = 6568 \text{\AA}$ having a passband of 19\AA (which is, in the case of the high-resolution Fabry Perot used here, just about twice the FSR).

The spectral resolution R_λ (or simply R) of the Fabry-Perot is provided by the following relation:

$$R_\lambda = pF \quad (4)$$

We thus need to know the interference order p and the effective finesse F . In practice, both parameters are roughly known and they are given by the manufacturer. The effective finesse needs nevertheless to be measured with accuracy. As explained in Appendix B, the finesse can be simply obtained dividing the FSR by the width of an arc line (e.g. the Ne I emission line 6598.95\AA) in a spectrum extracted from the calibration cube. The spectral resolution can be inferred from the width of a calibration arc line. The high (low) order Fabry-Perot for use with SAM has $p \simeq 609$ ($p \simeq 134$), at $H\alpha$ 6562.78\AA , a finesse $F \simeq 18.5$ ($F \simeq 30.5$) providing the spectral resolution of $R \simeq 11200$ ($R \simeq 4087$). Further information on the nature and on the determination of the Finesse is provided in section B3.3.

2.2.2 Taking calibrations and on-sky data

Once we know the FSR and finesse, then the optimal number of steps to scan a FSR has to be computed and the scanning sequence has to be defined (see also Appendix ??). For the observations of 30 Dor described in this paper, we decided to slightly oversample by 5-10%, choosing a scanning sequence of 40 steps with a scanning step of $\sim 12.8 \text{ km s}^{-1}$. The same number of channels must be used for on-sky and calibration scanning sequences, except for the one calibration cube that is obtained for determination of the FSR and finesse, which should be highly oversampled and should cover more than one FSR (see Appendix B).

Spectra of calibration arc lamps (those from the SOAR calibration unit) need to be taken in day time, ahead of the first observing night, for wavelength calibration and for computation of the several Fabry-Perot parameters that will define the observation strategy. Suitable interference filters should be illuminated by the calibration lamps, so that the final spectra will contain at least one arc line with similar wavelength to that of the observed emission-line ($H\alpha$ in our case, redshifted due to the velocity of the target). In our case, we chose to use the Ne I 6598.95\AA emission line for calibration and the best option was then to use the interference filter BTFI 6600.5/19.3, available from the BTFI filter set.

A reference wavelength calibration has to be repeated at the position of the object on the sky ideally at the start and at the end of each observation to account for possible mechanical flexures of the instrument as well as changes in the air index inside the FP plates due to temperature, pressure and humidity changes along the night.

In section 2.3 more details are given about a script that easily performs wavelength calibration of the data in a semi-automatic way.

We described above and in the Appendices how to compute the parameters necessary for setting up the Fabry-Perot and taking data. In practice, a Python program was written in order to define the acquisition sequence for a Fabry Perot data cube. It produces a shell script which has to be run each time the observer wants to take a on-sky observation or a calibration. The Python program is available in the SAMI machine and upon request. It is self explanatory and easy to use. The input parameters to the script are given in Appendix A.

We should note that a feature was included in the control software of SAMI in order to allow pausing/stopping while an exposure is being taken. This was necessary, given that there are laser interruptions that are mandatory during a given night. In addition, the

observation can be paused/stopped due to passing clouds. When the stop or pause button is pressed, the ongoing exposure is then finished and read out before the action (pause or stop) takes place.

A mode allowing 8×8 binning was needed for testing, at the commissioning, and this was then included in the software. A 4×4 binning mode (an option that already existed previously in SAMI but had not been implemented) was included in the new control software and has been used for the Fabry-Perot observations presented in this paper. Indeed, a binned pixel of size $0.18''$ still allows a good sampling of the best seeing and considerably increases the SNR per unit surface.

2.3 Data Reduction

The raw images obtained with SAM-FP are transformed into scientifically useful datacubes after following several procedures described below. Each FITS file obtained with SAMI has four extensions (the CCD controller has four amplifiers). Before the combination of the four FITS extensions into one FITS image, we combine the extensions into one single image, we estimate the background using the overscan region by fitting a 3rd degree polynomial along the columns' direction and subtracting it from each column. This procedure is followed for all data including bias, dark, flat, calibration and science files. After combining the extensions we then subtract the bias from the science frames and correct them by the normalized flats. It is important to note that SAMI's CCD has a strong instrumental feature that is not always present but can greatly affect the images. These are described as "arcs" in internal SAMI documents. They can be removed from the science images by subtracting suitably scaled dark images from the science frames, before flat fielding. It is, therefore, highly recommended that at least 10-20 darks are taken per night, with exposure times of 3-10 minutes, for this purpose. This feature was not seen in the data presented here, so no correction was needed. For science images with exposure times longer than several seconds, it is important to do cosmic ray cleaning. In our case, all procedures described above were performed using IRAF⁴, except for the procedure of combination of the FITS extensions, which was performed by a program kindly provided by Andrei Tokovinin.

The final calibration and science images were then converted into datacubes using a script called `mkcube2.py` using Numpy (van der Walt et al. 2011) for array operations and AstroPy (Astropy Collaboration et al. 2013) for FITS input/output. Having the calibration cube (in our case the Ne I datacube) in hand, the phase correction is performed with the main goal of re-arranging the spectral information in the science data-cube. As it is well known, the spectral information in each pixel, for Fabry-Perot data, is radially shifted with respect to the next, as one moves in the cube, along the spatial direction. This shift follows a parabolic surface centered on the Fabry-Perot optical center. In addition, because Fabry-Perot data are periodic, the spectrum repeats itself. Three steps are required for this phase correction: phase-map extraction, fitting and application. These steps have already been described previously in the literature, e.g. Atherton et al. (1982), Bland et al. (1987), Amram et al. (1989). The specific scripts used here are available to the

⁴ IRAF is distributed by the National Optical Astronomy Observatories, which are operated by the Association of Universities for Research in Astronomy, Inc., under cooperative agreement with the National Science Foundation.

Table 1. Journal of Perot-Fabry observations

Observations	Telescope	SOAR
	Instrument	Fabry-Perot inside SAM
	UT Date	March 18 th 2015
	FWHM of stars (laser corrected)	~0.5-0.7"
	Mean scanning lambda of 30 Dor obs	6568.78 Å
	30 Dor systemic velocity	267 km s ⁻¹
Interference Filter	Central Wavelength	6568 Å
	FWHM	19 Å
	Transmission	0.70
Calibration	Ne I reference line	6598.95 Å
	Central lambda of filter used to select Ne line	6600.5 Å
	Width of filter used to select Ne line	19.3 Å
Fabry-Perot	Company and ID	ICOS ET-65
	Interference Order	609 @ 6562.78
	Free spectral range at H α	10.8 Å(492 km s ⁻¹)
	Finesse	18.5 at 6598.95 Å
	Spectral resolution at H α	11200
Sampling	Number of Scanning Steps	40
	Sampling Step	0.28 Å(12.8 km s ⁻¹)
Detector	e2v	CCD 4096 × 4112
	Total Field of View	120" × 120" ^a
	Pixel size	0.18" ^b
	Readout noise (unbinned)	3.8 electrons
	Gain	2.1 electrons/ADU
Exposures times	Total on-target exposure	80 minutes
	Total exposure time per channel	120 s

^a The field of view is limited to 2×2 arcmin² by the interference filter used.

^b The pixel size of SAMI is 0.045. Pixels were binned 4x4.

community⁵. All the scripts can be executed via command line and their documentation can be accessed via the “–help” argument. The phase map is derived from a calibration cube using the program phmtractor.py. Adjustment of the phase map to a parabolic surface is performed with phmfit.py. We finally use phmapply.py to unwrap the spectral information bringing each pixel in the spectrum to the correct frame. At this point we have a data cube where each frame represents one wavelength (modulo the FSR, given the cyclic nature of the Fabry-Perot device).

For wavelength calibration we use two calibration cubes taken at different wavelengths. In fact, as explained in section 2.2.2, only one cube would be necessary for calibration but a second one is taken for interference order checking. In our case we used a Ne Lamp with two filters that contained the following lines respectively, 6598.95Å (BTFI filter 6600.5/19.3) and 6717.04Å (BTFI filter 6745.5/38.6). The latter is only for order checking. When using the script, the calibration cube (in our case the 6598.95Å data cube) has to cover more than one free spectral range so that the line will appear in two different orders and the second cube (in our case the 6717.04Å data cube) can cover one free spectral range only. We also need to extract a 1D spectrum from these cubes at the center of the rings. Section 5.9 of Atherton et al. (1982) describes in detail the procedure for wavelength calibration of tunable filter images, which has been adapted for our use. The script fpwcal.py was written to make the wavelength calibration automatic. The script is interactive and self explanatory.

The cube is then ready for night-sky line subtraction and derivation of the monochromatic, velocity and dispersion maps.

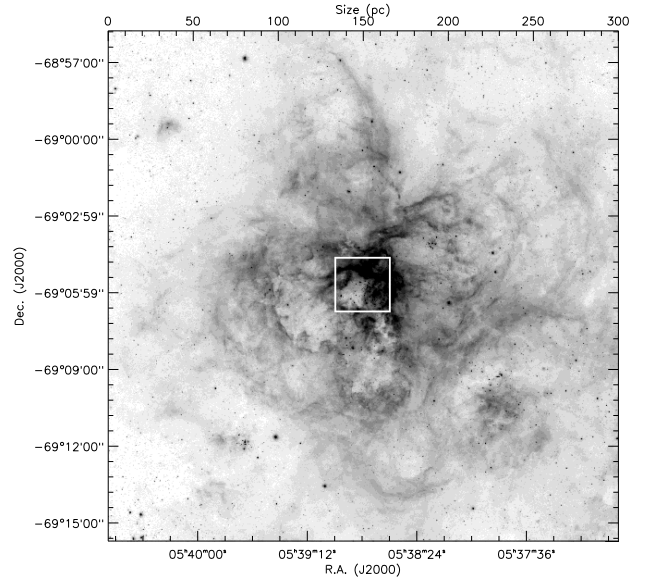


Figure 2. H α image taken at T80-South during comissioning of its wide-field camera, which provides images with a field of view of 1.4×1.4 degree². The large image above covers a $\sim 20 \times 20$ arcmin field centered on R136 and the white box indicates the central 2×2 arcmin² of the image, observed with the Fabry-Perot ICOS ET-65.

3 OBSERVATIONS OF 30 DOR

The observations of 30 Doradus were taken on UT date March 18th, 2015, with the high-resolution scanning Fabry-Perot interferometer described above, placed inside SAM, fed to SAMI. Although the

⁵ <https://github.com/b1quint/btfi>.

total field of view of the instrument is 3×3 arcmin², due to the smaller size of the H α interference filter, the useful field of view was 2×2 arcmin². We used a 2×2 inch² interference filter from the Cerro Tololo list, centered at 6568 Å (filter 6568-20⁶), with a FWHM of 19 Å and with transmission of $\sim 70\%$ (according to the list of CTIO filters). The free spectral range of the interferometer (492 km s^{-1}) was covered in 40 scanning steps. The setup and observing details are summarized in Table 1.

The observations were taken under photometric conditions. The seeing during the observations varied between 0.7 and 0.8 arcsec. GLAO correction lead to an improvement of spatial resolution and flux of up to ≈ 2 , yielding a FWHM of 0.5-0.7 arcsec. The spatial resolution of the cubes was then determined by the laser corrected FWHM with a mean value of 0.6" or 0.15 pc. The instrumental profile, as measured from Ne calibration lamp lines was 0.586 Å or 26.8 km s⁻¹, which corresponds to a spectral resolution of about 11200 at H α . The last four channels were taken after a laser interruption of a few minutes and after some technical problems which took about 45 minutes to be fixed. The data for the last channels were taken under higher airmass (> 1.5) and slightly worse seeing (0.7" after correction). This, however, represented only 10% of the data and it did not degrade significantly the quality of the cube as a whole.

Fabry-Perot observations are usually taken with short exposure times and in a number of sweeps, to account for transparency and seeing variations. However, given that we are observing with a classical CCD (not an EMCCD nor a photon-counting camera), we chose to make just one sweep of 40 channels and with fairly long exposure times of 120 seconds each, to minimize the readout noise (see also section A3.4). The night sky lines have been identified by plotting a histogram of wavelengths and picking the most frequent values (given that the sky lines are present in every pixel). Knowing their wavelengths and intensities, night sky lines were then subtracted. Alternatively, a nebulae-free datacube beside the object (new pointing) could have been observed to directly subtract the night sky lines (see section A4.2) but this was not done in the case of these 30 Doradus observations.

Figure 2 shows with a white square the region observed in the present study. The background image is an H α observation taken during commissioning of the robotic telescope T80-South⁷. A cut of 20×20 arcmin² centered on 30 Dor was extracted from the T80-South image and it is shown in Figure 2. The area of 2×2 arcmin², observed with the Fabry-Perot, is indicated with a white box. The bright star cluster R136 is included in the area observed.

4 DATA ANALYSIS

4.1 Comparing Fabry-Perot data with previously published H α kinematic data of 30 Dor

The Fabry-Perot H α data cube of 30 Doradus was compared with a data cube obtained with the FLAMES instrument at VLT and the Giraffe spectrograph in MEDUSA mode, published by Torres-Flores et al. (2013). About 900 fibers were used to obtain kinematic information over a field of view of $10' \times 10'$, centered on R136,

with a spectral resolution of $R \sim 17000$ (compared to $R \approx 11200$ for the Fabry-Perot data). The distance between each fiber for the FLAMES/VLT setup was 20 arc sec. In the case of the Fabry-Perot data, we observed a FOV of $2' \times 2'$, with a pixel scale of 0.18 arcsec and with a median FWHM of 0.6 arcsec. Therefore, the spectral resolution of the Fabry-Perot data is about 30% poorer but the spatial coverage or spatial resolution (or more precisely, the number of independent measurements) is more than 30² times higher than that for the VLT data (which has a measurement taken with a MEDUSA fiber of 1.2" diameter at every 20 arcsec). For this reason, and in order to do a fair comparison, we have extracted from the Fabry-Perot data, squared regions of $1.1'' \times 1.1''$ that are placed at the same positions as the MEDUSA fibers were. For each region we have co-added the profiles, to get a mean H α profile of the region, which can then be compared with the MEDUSA fiber data. In the upper panel of Figure 3 we show the FLAMES/VLT H α profiles taken from Torres-Flores et al. (2013) and in the lower panel those taken from the Fabry-Perot data, where all profiles have been normalized to the integrated flux of the line in each specific region or fiber. In both cases the background image corresponds to an H α observation of 30 Doradus taken with the ESO NTT/EMMI instrument under program 70.C-0435(A).

Inspecting the Fabry-Perot data (lower panel of Figure 3) narrow- and broad-emission-line profiles can be seen at different regions of the nebula. Such profiles have been previously reported by Chu & Kennicutt (1994) and others. The broadest profiles can be seen to the East of R136, and they may be associated with a cavity (so called "Christmas Tree")⁸ located to the Southeast of R136. On the other hand, the narrow profiles are associated with H α filaments. Comparing the upper and lower panels of Figure 3 we are able to check if the Fabry-Perot observations reproduce well the VLT/FLAMES results. Despite having a lower spectral resolution, it is clear that the Fabry-Perot H α profiles display quite similar shapes to the previously published data. For instance, from top left, boxes (3,2), (3,3) and (2,3) display the same blue component in both cases. Also, the shapes of the H α profiles in boxes (4,4), (4,5) and (5,4) are similar in both cases. In addition, the behavior of the emission line profiles in the central region of the "Christmas tree" is also consistent with results in the literature (e.g. Chu and Kennicutt 1994, Melnick et al. 1999).

In order to do a fair comparison between the SAM-FP and VLT/FLAMES data cubes of 30 Dor, we centered the integrated H α emission line from the SAM-FP at the exact radial velocity of the integrated H α emission line profile of the VLT/FLAMES cube, over the region of overlap. The procedure undertaken to match the radial velocities of both data sets was the following. First, we derived a sub-cube of the VLT/FLAMES H α data cube, which covered the same 2×2 arcmin² field of view of the SAM-FP observations (see Figure 3). We derived the integrated H α profile for this region and fitted a single Gaussian. We obtained a central wavelength of 6568.72 Å, which corresponds to 270.7 km s^{-1} . We note that this value is slightly higher than the radial velocity derived by Torres-Flores et al. (2013) of 267.4 km s^{-1} , but that was for the whole VLT data cube. We then obtained the integrated H α profile of the SAM-FP data cube, fitted a Gaussian to it and found a central wavelength

⁶ <http://www.ctio.noao.edu/noao/sites/default/files/instruments/filters/6568-20.gif>

⁷ T80-South is an 80-cm telescope mounted at Cerro Tololo, which has a CCD camera with a $9.2k \times 9.2k$ pixel² CCD yielding a 1.4×1.4 degree² field of view (with 0.55-arcsec pixels). The telescope was built by the companies AMOS and ASTELCO and the CCD camera by Spectral Instruments.

⁸ This cavity has distinct identifications given by different authors, e.g. it is called region "H" by Melnick et al. 1999 and "Christmas tree" by De Marchi et al. (2014). It is a region with an additional extinction component as compared to the neighboring regions and it resembles the silhouette of a Christmas tree.

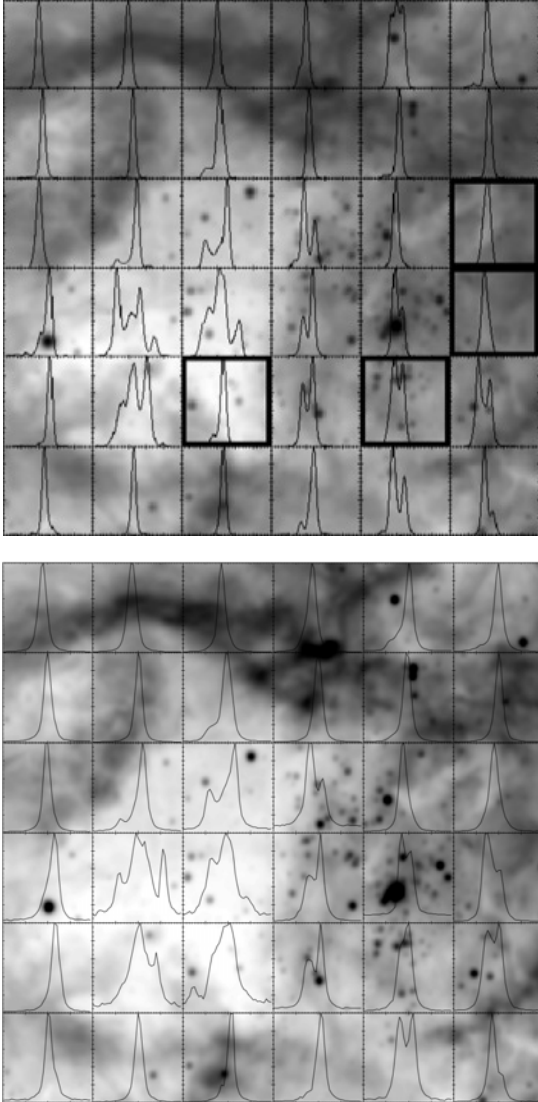


Figure 3. Upper panel: Central region of 30 Doradus (extracted from fig. 3 of Torres-Flores et al. 2013). Each profile corresponds to the $H\alpha$ emission line obtained with the MEDUSA mode of the Giraffe/FLAMES instrument, at VLT. According to fig. 3 of Torres-Flores et al. (2013), thick-lined boxes indicate positions for which no spectra were available (broken fibers) and profiles were then interpolated, i.e. the average of the nearest “pixels” (fibers) were taken, to fill these gaps. Lower panel: extracted Fabry-Perot data in the same area. The plots correspond to the average profiles of the Fabry-Perot data over a square of $1.1 \times 1.1 \text{ arcsec}^2$ in the center of each box, in an attempt to mimic the Giraffe/FLAMES observations. In both panels the background image corresponds to an $H\alpha$ image of 30 Doradus taken with the ESO NTT/EMMI instrument.

that we matched to 6568.72\AA . Therefore, the zero point of the radial velocity of our dataset is tied to that derived by Torres-Flores et al. (2013), for the same region.

Once we have compared both data sets and they show good general agreement, we proceed to analyse the Fabry-Perot data, for which we have continuous spectroscopic information with a scale of 0.18 arcsec (0.045 pc).

4.2 Computing the monochromatic map and flux calibration

At first we attempted to create the monochromatic map of the 30 Doradus region by fitting a single Gaussian to each pixel (see section 4.3 for the Gaussian fitting process). However, we concluded that the fit of single Gaussians to the often-encountered multiple $H\alpha$ profiles brought no meaningful information to the monochromatic map, given the complex profiles of the nebula. We, therefore, used the 2D collapsed data cube as the $H\alpha$ monochromatic map (shown in Figure 5), assuming that the contribution from the spectral continuum is negligible (and we do measure a very low continuum for the whole region). The Gaussian fits were still used for the velocity and dispersion maps (Figures 6 and 7), as described in the next subsection, given that in those cases it was still interesting to have the position of the main velocity peak at each pixel (in the case of the radial velocity map) and an indication of the width of the profile or presence of multiple profiles (in the case of the dispersion map).

In order to flux calibrate the SAM-FP data of 30 Doradus, we have used an archival HST image of this region, which was observed with the WFC3 and using the narrow-band filter F656N. We used the task `PHOT` in IRAF⁴ to measure the instrumental fluxes of 31 regions located across the field (which were located inside the same FoV of the SAM-FP $H\alpha$ image), inside an aperture of 3 arcsec radius. These instrumental values were converted into physical fluxes by using *PHOTOFIT* (which is the so-called inverse sensitivity)⁹, $F=1.78462 \times 10^{-17} \text{ erg cm}^{-2} \text{ s}^{-1} \text{ \AA}^{-1}$ and the FWHM of the filter of 13.9 \AA ¹⁰. Finally, each measurement was divided by the area within which the flux was estimated. For the SAM-FP 2D collapsed image, we obtained the number of electrons per seconds for the same regions defined for the HST image, inside the same apertures, using the same procedure (here we use the gain and exposure times listed in Table 1 to transform counts in electrons/s). In Figure 4 we show the result of this analysis, where a dashed-dotted line represents a linear fit to the data, which provided us with a slope of $1.32 \times 10^{-15} \text{ erg cm}^{-2} \text{ electrons}^{-1}$ (we note that this value is consistent with the slope derived by forcing the zero point to zero, $1.38 \times 10^{-15} \text{ erg cm}^{-2} \text{ electrons}^{-1}$). Then, we have calibrated the SAM-FP 2D image, here called monochromatic image, by using this coefficient (as can be seen in Figure 5). We note that the use of the collapsed image avoids possible problems that arise from the use of a single Gaussian fitting in regions where the $H\alpha$ profile displays multiple peaks (for example, around expanding structures).

4.3 Fitting Gaussians to the $H\alpha$ data cube

We have fitted a single Gaussian to each observed $H\alpha$ profile in 30 Doradus, by using the code `FLUXER`, an interactive routine in IDL¹¹. The code `FLUXER` uses the package `MPFIT` to fit a modeled Gaussian to the observations, which allows us to determine the center, width and flux of the Gaussian. In this case, the center can give us information regarding the radial velocity of the gas and the width can be used to characterize the overall complexity of the $H\alpha$ profiles, indicating where there may be superposition of different kinematics structures and turbulence. In this manner we then computed the radial velocity and dispersion maps for the region.

The results of the Gaussian fitting process are shown in Figures

⁹ http://www.stsci.edu/hst/wfc3/phot_zp_lbn

¹⁰ <http://www.stsci.edu/hst/wfc3/documents/ISRs/2003/WFC3-2003-02.pdf>

¹¹ This routine was written by Christof Iserlohe, <http://www.ciserlohe.de/fluxer/fluxer.html>

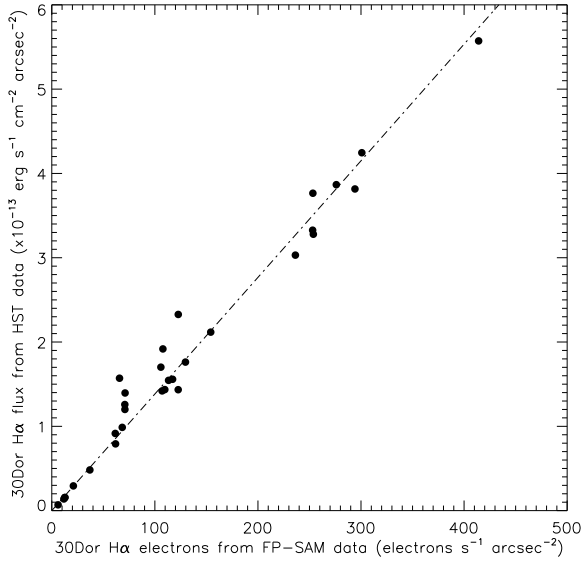


Figure 4. Flux calibration of the SAM-FP data of 30 Doradus using an archival HST image of the same observed region. In the x-axis instrumental fluxes of 31 regions located across the FP field, within an aperture of 3 arcsec in radius, are computed and plotted and in the y-axis the corresponding fluxes for the same regions obtained from the HST image are given.

6 and 7, where we show the velocity field and the velocity dispersion map, respectively. Although several H α profiles show a complex shape (e.g. multiple peaks), the use of a single Gaussian fit is still useful to understand, from a general point of view, the kinematics of this nebula, as it will become clear in the next section.

In a few specific cases it is necessary to fit several Gaussians to the profiles, as it is the case, for example, when measuring the expansion velocity of a newly found bubble in the center of 30 Dor in section 5.5. For that, we used the code PAN (Dimeo 2005) to fit multiple (and also single) Gaussians to the observed profiles. This code, which runs in IDL, allows the user to define interactively multiple Gaussians, estimating the flux, width and center of each component.

5 RESULTS

In this section we describe the main kinematic features found in the H α Fabry-Perot data cube of 30 Doradus.

The most striking result as we inspect the cube of 30 Doradus is the diversity of profiles on the smallest scales. This is exemplified in Figure 8 for an area of 9×9 arcsec. Here, each square corresponds to a profile binned 5×5 pixel², i.e. over a 0.9×0.9 arcsec² area (which corresponds to 0.23×0.23 pc²). The profiles change abruptly between neighbouring boxes, with components appearing and disappearing in a fraction of a parsec scale.

A detailed analysis of the kinematics of different specific regions in the whole $2' \times 2'$ is deferred to a future paper.

5.1 H α emission

In Figure 5 we show the flux calibrated H α monochromatic map of the central region of 30 Doradus recovered from the Fabry-Perot data. Most of the features visible in this image have already been

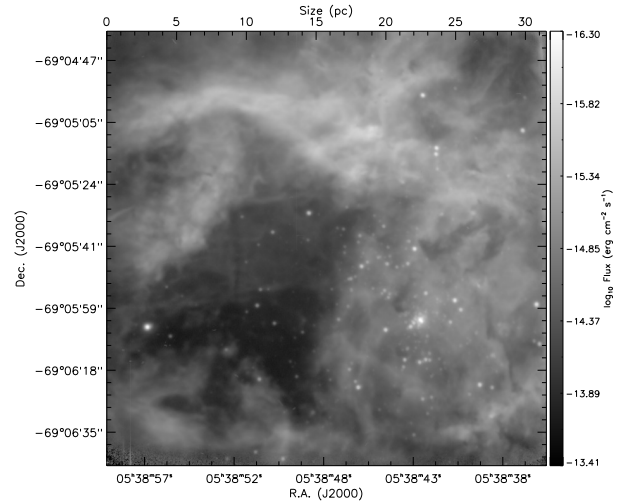


Figure 5. H α monochromatic map of the central region of 30 Doradus, derived from the Fabry-Perot data cube, as explained in the text. This map is flux calibrated (see Section 4.2).

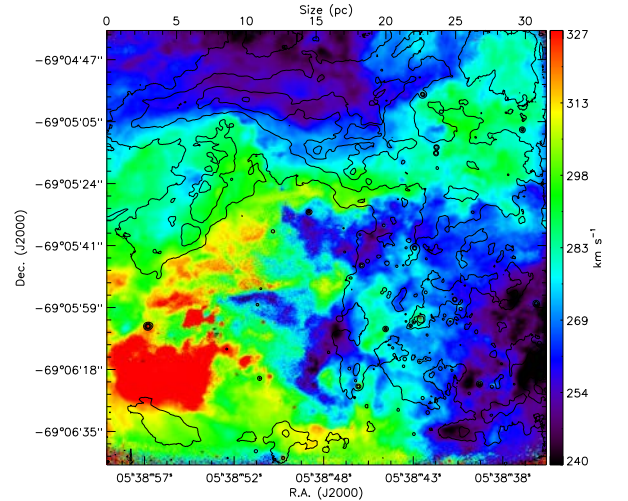


Figure 6. Velocity field for the same region as shown in Figure 5. The scale is shown in km s⁻¹. The contours show the following flux levels (from the monochromatic map): 8×10^{-16} , 2×10^{-15} , 5×10^{-15} , 8×10^{-15} erg s⁻¹ cm⁻².

studied in the literature. For instance, the bright Northeast and a portion of the West filaments described as ionization fronts by Rubio et al. (1998) and Pellegrini et al. (2010) are clearly outlined. Many dark clouds are easily seen in contrast against the bright nebula, for example the “stapler-shaped” dark cloud (Walborn, Barbá & Sewilo 2013). Another structure seen is the dusty main cavity or “Christmas tree”, which was detected by previous studies (e.g. Chu & Kennicutt 1994, De Marchi & Panagia 2014).

5.2 Velocity field

In Figure 6 we show the velocity field for the central region of 30 Doradus. This map is derived by fitting a single Gaussian to each observed profile, often when multiple kinematic components are

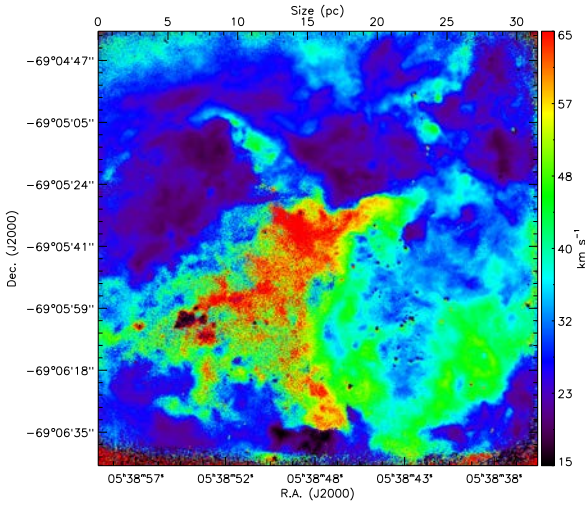


Figure 7. Velocity dispersion map for the same region as shown in Figure 5. The map was corrected by instrumental and thermal widths.

present. This averages out the profiles and it is not the best way to reveal the presence of expanding structures. However, the velocity field can still give us a general idea about the kinematics of the region.

One of the most intriguing features in this map corresponds to the middle region of the main cavity, or “Christmas tree” (R.A. \sim 05h 38m 50s, Dec \sim -69d 05m 52s). Around this location there is an abrupt change in the values of radial velocities, of $\approx 40 \text{ km s}^{-1}$, suggesting the existence of a complex kinematic structure. This map again shows that the kinematics in 30 Doradus changes in small spatial scales.

The structure of the velocity field poorly correlates with the $H\alpha$ distribution, in contrast with the velocity dispersion map, which strongly correlates with the monochromatic map (see next section and Figure 7). In the velocity field, we observe a global velocity gradient of $\approx 80 \text{ km s}^{-1}$ from Southeast to North and Southeast to West. In addition, a component which either mimics or is a real continuous velocity component is observed from Southeast to Northwest (at $\approx 295 \pm 10 \text{ km s}^{-1}$). Around this axis, in a conical structure, the gas is approaching at lower mean velocity ($\approx 260 \pm 10 \text{ km s}^{-1}$) and around the “trunk” of the Christmas tree a higher velocity component ($\approx 320 \pm 10 \text{ km s}^{-1}$) is moving away from the observer. From a geometrical point of view, this all suggests that we are observing a conical expanding structure rotating around an axis that runs from the Southwest to the Northeast, but none of these motions are smooth.

5.3 Velocity dispersion map

In Figure 7 we show the velocity dispersion map for the studied region. This map has been corrected by instrumental and thermal widths, $\sigma_{inst} = 11.3 \text{ km s}^{-1}$, $\sigma_{th} = 9.1 \text{ km s}^{-1}$, respectively. The latter value was estimated by assuming an electronic temperature of $T_e = 10^4 \text{ K}$ in the expression $\sigma_{th} = (k T_e / m_H)^{1/2}$. This map was derived from a single Gaussian fit, thus, regions having the largest σ can be associated with those where two or more emission line profiles are superimposed at different velocities. This map is then a useful tool to search for expanding structures. Inspecting Figure 7, we note that most of the high surface brightness regions (see Figure

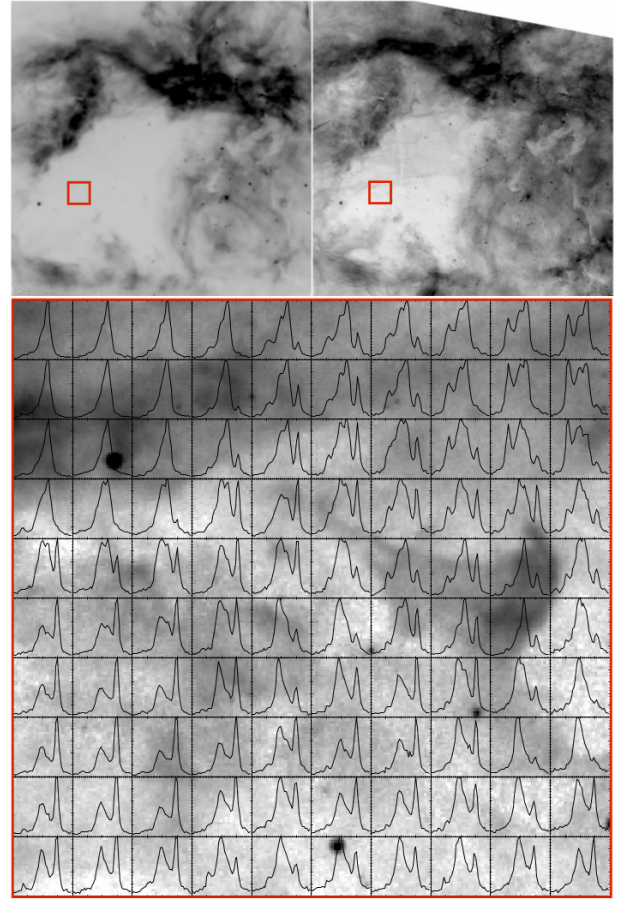


Figure 8. Profiles of one selected area of 30 Dor. Top left panel: $H\alpha$ image extracted from channel 21 of the Fabry-Perot data cube (see Figure 9 for a color version of this channel). The red square indicates the region whose profiles are shown in the lower panel. Top right panel: HST $H\alpha$ image of the same region displayed on the top left. Bottom panel: $H\alpha$ profiles over a 5×5 array of binned pixels. Each “pixel” is 0.9 arcsec (0.23 pc) on a side. The purpose of this Figure is to show the diversity of profiles in a small area of only $9 \times 9 \text{ arcsec}^2$ ($0.23 \times 0.23 \text{ pc}^2$). This diversity is typical of the whole area observed. Note that the profiles can be easily traced from one pixel to the next.

5) display narrow profiles ($\sigma \sim 20\text{--}30 \text{ km s}^{-1}$). On the other hand, low intensity regions display broad profiles ($70\text{--}80 \text{ km s}^{-1}$), which arise from unresolved emission line components. In some cases the emission line profiles can be resolved, giving larger widths. In addition, this area also displays abrupt changes in the number of components, intensity and radial velocities of the ionized gas. Comparing Figure 7 with Figure 5 we can see that the regions that display the largest widths correlate with the “Christmas tree” (see Figure 5). The detailed kinematics of this region will be described in a future paper.

5.4 A channel view of the data cube

In order to better display the kinematics of the inner region of the 30 Doradus Nebula, in Figure 9 we show the more relevant (in terms of flux) channel maps of the $H\alpha$ data cube (channels 10 to 29, 149.0 to 392.2 km s^{-1}). Starting from channel 16 (225.8 km s^{-1}) we can see some emission associated with blue shifted gas. Between channels 18 (251.4 km s^{-1}) and 20 (277.0 km s^{-1}) we have the peak of the emission. Also, the cavity or “Christmas tree” clearly appears in

several channels. This cavity partially disappears in channels 24 to 26 (328.2 km s^{-1} to 353.8 km s^{-1}). It is associated with broad, multiple profiles, as can be seen in Figure 7.

From the channel maps shown in Figure 9, one can see the presence of an expanding bubble identified here for the first time in the lower right of channels 20 to 25 (277.0 km s^{-1} to 341.0 km s^{-1}). The presence of this bubble is not obvious in Figure 6 but it can be identified as a region of broader profiles (i.e. larger widths - when using a single Gaussian fit) in Figure 7.

5.5 Identification of a bubble in the center of 30 Dor

The good spatial coverage and resolution of SAM-FP together with the reasonably good spectral resolution allows us to find new small-scale kinematic structures, which can not be easily identified in previous sparse multi-fiber data or in long slit studies, where the positioning of the fibers and the position angle of the longslit can bias the detection of these kinematic structures. Given that the aim of this paper is to show the capabilities of SAM-FP, here we show an example of an expanding structure, which appears when inspecting the $\text{H}\alpha$ data cube.

At the top panel of Figure 10 we show a slice of the Fabry-Perot data cube, which is centered at velocity 315.4 km s^{-1} (channel 23). The white circle indicates the location of an expanding bubble centered at R.A. $\sim 05^{\text{h}} 38^{\text{m}} 42^{\text{s}}$, Dec $\sim -69^{\circ} 06' 23''$.

Torres-Flores et al. (2013) identified a large bubble that encompasses this region (their region 8) and also includes the central cluster R136. However, they had a poor spatial coverage of one spectrum each 20 arcsec. With the present dataset we can more precisely identify the location and size of this expanding bubble. In Figure 10 it is possible to see arc-like features, which delineate the structure, approximately following the contours of the white circle (top panel). The kinematic signature of this source is shown in the bottom panel of Figure 10, which is the result of adding all the $\text{H}\alpha$ profiles that are enclosed inside the white circle (top panel). In this plot, we can see a double-peaked profile, which is typically associated with expanding structures. In order to quantify the expansion velocity of this structure, we have fitted two Gaussians to the profile (plus a low-intensity continuum emission). This procedure allows us to derive the radial velocity of both components. Under the assumption that these components are associated with the approaching and receding sides of the expanding bubble, the expansion velocity of the bubble can be estimated as $V_{\text{expansion}} = (V_{\text{receding}} - V_{\text{approaching}})/2$. This exercise yields a velocity of $V_{\text{expansion}} = 29.1 \text{ km s}^{-1}$. The radial velocity of the baricenter of the bubble, $(V_{\text{receding}} + V_{\text{approaching}})/2$, is 273.4 km s^{-1} . Considering that the bubble has a projected radius of 22 arcsecs or 5.6 pc, we can speculate that this structure has been expanding for a period of $\sim 180,000$ years, assuming a constant and uniform expansion.

The ionizing source (or sources) associated with this expanding bubble cannot be easily identified using FP data alone, given that the continuum emission is poorly sampled in the data-cube. Inspecting the population of massive stars in the central $10'' \times 10''$ (or $2.5 \times 2.5 \text{ pc}^2$ box) of the proposed bubble, we have two remarkable stars, indicated in Figure 10: the blue supergiant Melnick 38 (VFTS 525, B0 Ia, Walborn et al. 2014) and the very massive spectroscopic binary VFTS 512 (O2 V-III, Walborn et al. 2014). These stars are located $2.7''$ and $2.4''$ from the center of the bubble, respectively, and they have different reasons to be the source of the expanding nebula. In the case of VFTS 512, we could be witnessing the birth

of a pristine young bubble produced by a powerful wind and UV-radiation of a very young massive star. In the case of Melnick 38, the origin of the nebula could be related to advanced evolutionary stage of a blue supergiant. Walborn and Blades (1997) described that in 30 Doradus at least five distinct populations of massive stars are coeval, from an embedded population of massive stars (see also Rubio et al. 1998, Walborn, Barbá & Sewilo 2013), the Orion Nebula-like population to a more evolved sparse population, composed by blue and red supergiants, the Sco-Cen OB association-like population. Naze et al. (2001) searched for pristine bubbles in two very young HII regions of the LMC, N11 and N180. They discovered a very small bubble around the multiple star PGMW 3120, with a composed spectral type of O5.5V((f)), which is described as a very young asymmetric bubble by Barbá et al. (2003).

The new expanding bubble found in this work is located close to the star cluster R136 (its center is $5.6''$ South of R136, in projection). Although the mechanical feedback of R136 stars could disrupt any small-scale kinematic structure located in its environment, this does not seem to be the case here, given the apparently smooth shape of the bubble contours and its distinct kinematics. Probably this bubble is not located immediately next to R136 and the spatial coincidence we see is just a chance alignment, in the line of sight. Projection effects should be taken into account in the identification and analysis of bubbles.

5.6 The integrated $\text{H}\alpha$ profile

A few studies to date have suggested that the integrated $\text{H}\alpha$ profile of 30 Doradus is composed by a broad component, due to a low-intensity emission, superposed to a narrow, high-intensity component. This may be caused by the sum of expanding structures or may be the result of the superposition of a number of narrow, low-intensity components with different radial velocities. We expect the broad component to be quite faint and therefore a detailed and careful analysis and modeling of the line profiles needs to be done. While this problem is outside the scope of the present paper, it is still interesting to measure the width of the integrated emission line of the whole region observed, to compare with that measured in the previous work of Torres-Flores et al. (2013). For this, we stacked all profiles of the 30 Doradus cube (a $2 \times 2 \text{ arcmin}^2$ region). We then fit a single Gaussian to the integrated $\text{H}\alpha$ profile, which is shown in Figure 11. The black continuous line in this Figure corresponds to the integrated observed profile, while the red dashed line is the modeled Gaussian (which was obtained by using the code PAN in IDL). We corrected the profile for instrumental and thermal broadening, in a similar way done for the velocity dispersion map and we then computed its dispersion to be $\sigma \sim 33.6 \text{ km s}^{-1}$. This value is higher than the value found by Torres-Flores et al. (2013) of $\sigma = 26.5 \text{ km s}^{-1}$, but that was for a much larger region of $10' \times 10'$ centered on R136. These values are consistent, given the uncertainties due to different resolutions and different sizes of the regions used in the determination.

In a forthcoming publication (Torres-Flores et al. in preparation) we will take into account the shape of the Fabry Perot profile (Airy Function) to correctly investigate the presence of wings in the integrated $\text{H}\alpha$ profiles, after bringing all different radial velocity profiles to a common zero point velocity.

5.7 Visualizing the $\text{H}\alpha$ data cube in 3D

3D visualization of the $\text{H}\alpha$ Fabry-Perot data cube of 30 Doradus can help us understand the structure and kinematics of the nebula.

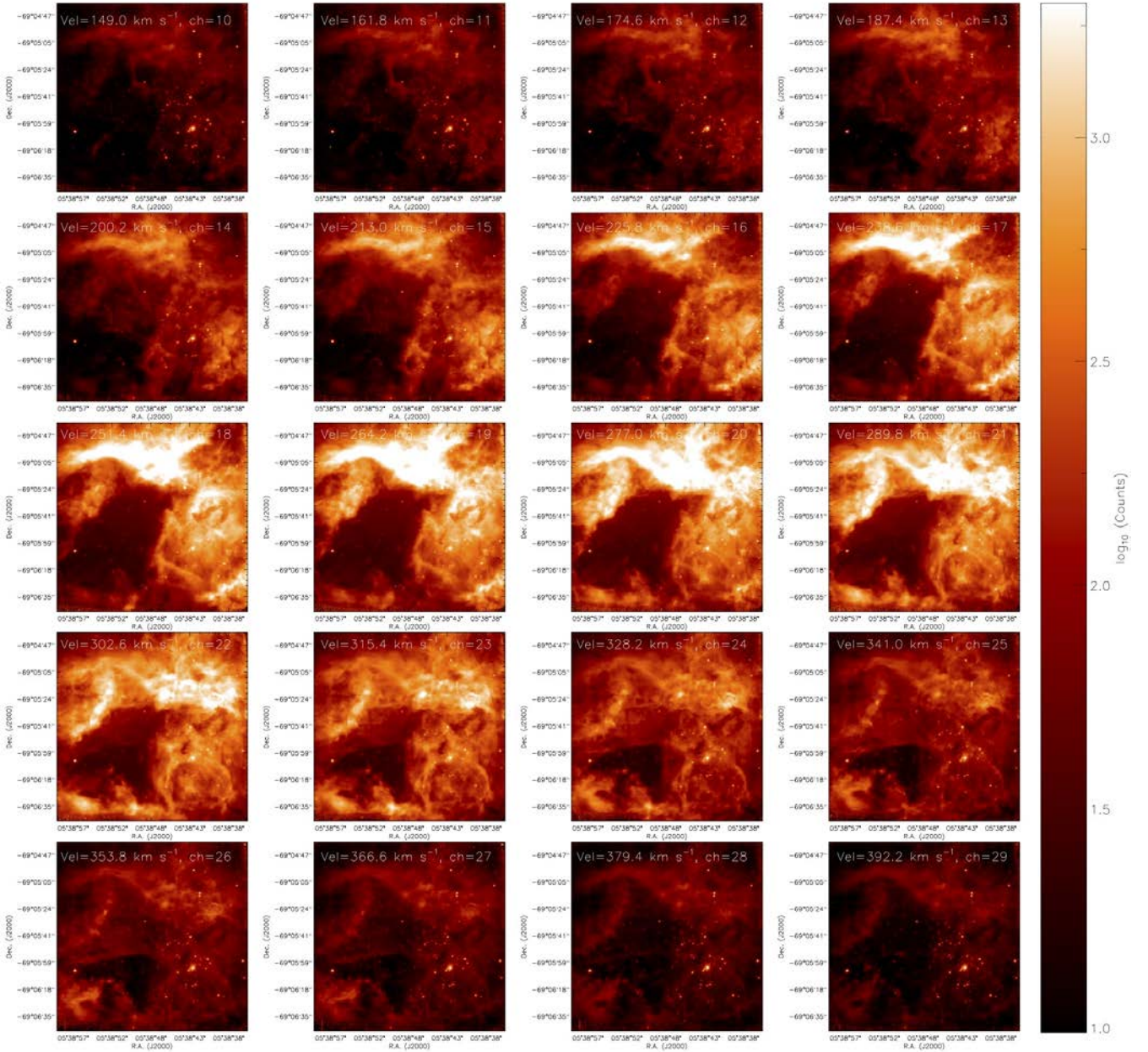


Figure 9. Channel maps for the $H\alpha$ data cube of 30 Doradus. We show here the 20 channels (of the 40 channels observed) with most emission. The Northeastern filament can be best seen in channels 18 and 19 as a bright emission on the upper parts of the frames. The “Christmas tree” can be seen in most channels, for an example, on channel 21, as the dark feature in the Southeast of the frame. Mean velocity of the channel is shown on the top of each stamp.

Figure 12 shows one such 3D representation, where right ascension, declination and velocity (wavelength) of 30 Dor are plotted. In order to highlight small scale kinematic features, the wavelength axis has been resampled to 350 channels (instead of the original 40 channels). The Figures were produced with GLnemo2, a software that allows moving the data cube in different directions. These directions are indicated by arrows in the right-hand corner of each panel, where the red, green and blue arrows correspond to right ascension, declination and velocity (wavelength), respectively. Depending on the angle along which the data cube is seen, we can obtain from a face-on (0-degree view) image to a position velocity map (90-degree view). Figure 12 shows a 3D view with rotation around the

declination axis. Here we show a frontal view, then a 45-degree, a 70-degree and a 90-degree view of the system. Regions of greatest intensity are shown in red while blue regions are those with lowest intensity. The straight lines are the stars, which help constructing the 3D view.

The contours of the cavity or “Christmas tree” are very well defined in the first three panels of Figure 12 (all except the 90-degree) given the contiguous coverage of emission over the field. In the top, a frontal view is shown, where several low-luminosity structures can be seen within the cavity. These are filaments being ejected in the line of sight. They were seen by both Melnick et al. (1999) and Chu & Kennicutt (1994) in 2D images and long-slit

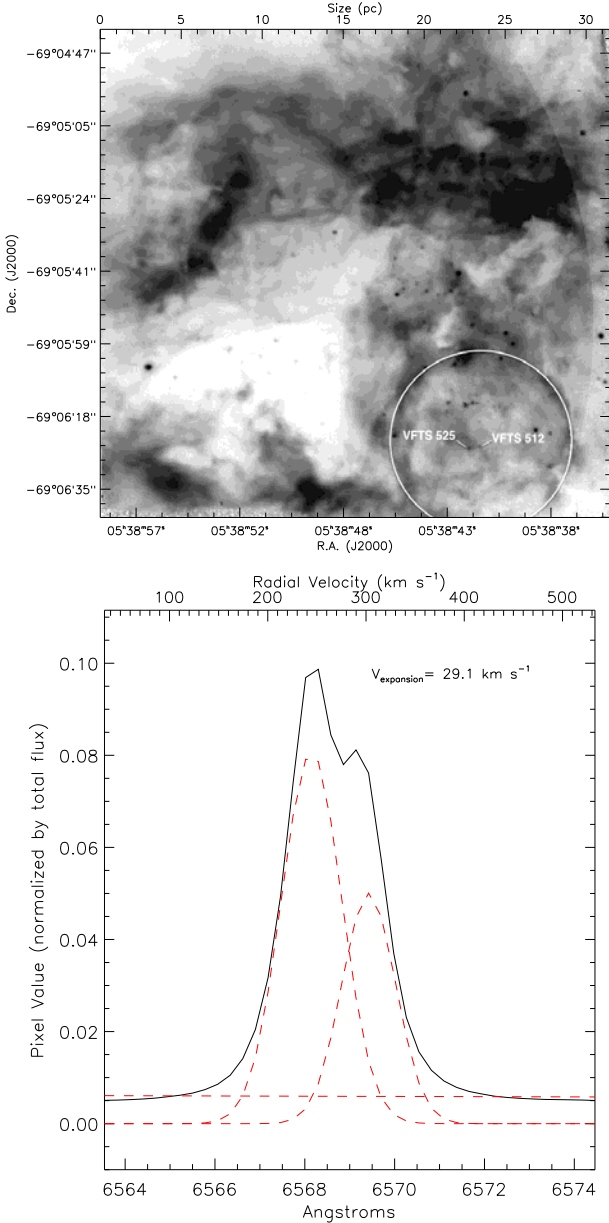


Figure 10. Top panel: channel 23 (315.4 km s^{-1}) of the 30 Dor data cube, where the white circle indicates the location of the expanding bubble. The blue supergiant Melnick 38 and the very massive spectroscopic binary VFTS 512 are indicated. Lower panel: integrated $H\alpha$ profile for the region contained within the white circle shown in the top panel. Red dashed lines represent two Gaussian components plus a continuum component, which can be identified as a horizontal line, with a value of ~ 0.006 .

spectra as numerous gas blobs moving with more than 100 km s^{-1} with respect to the system. This suggested to these authors that this is a region where expanding wind-driven shells undergo break-out. These kinds of structures were also identified by Redman et al. (2003) in another region of 30 Doradus. In this sense, a detailed analysis of $H\alpha$ SAM-FP data will be extremely valuable in order to determine the main mechanism producing these discrete knots.

The different radial velocities across the nebula shown in the 90-degree cut (the position-velocity diagram) also indicate the existence of several kinematic structures, possibly parts of one or more expanding shells.

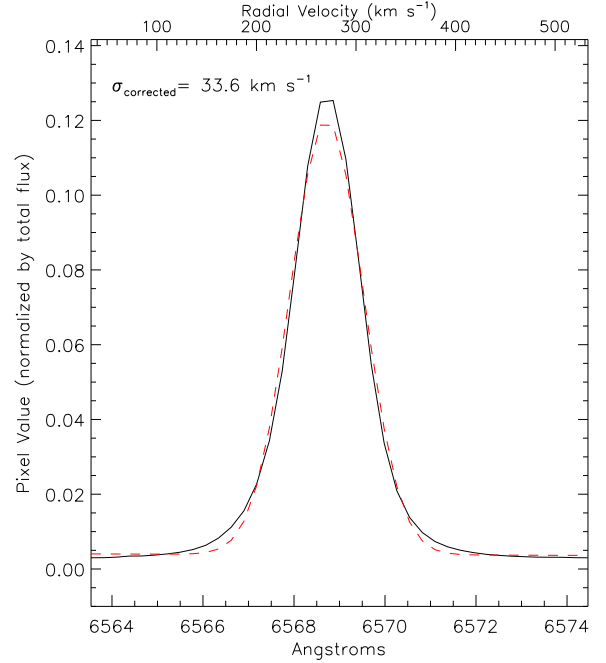


Figure 11. Integrated $H\alpha$ profile of 30 Doradus, derived from the whole data cube (black continuous line). The red dashed line corresponds to a single Gaussian fit to the observed profile. In the top left corner we list the value of the width (σ) of the integrated profile, which has been corrected by instrumental and thermal widths.

Another remarkable feature of Figure 12 is the clear indication that the Northeast filament (Rubio et al. 1988, the filament that runs horizontally on the top part of the Figure) has a different velocity than the Eastern filamentary loop (also identified as ionization front 2, or “if2”, Pellegrini et al. 2010). If we measure the difference in velocity between the channel where the Northeast filament is brightest and that where the Eastern loop is brightest, we find 37 km s^{-1} . We consider the error to be \pm one channel, or $\sim 13 \text{ km s}^{-1}$.

There is a clear velocity gradient of the Northeastern filament, with increasingly more negative velocities running from West to east. This can easily be seen by blinking the channels, one after the other, around channels 16-21. It can also be clearly seen in the 4th panel of Figure 12, which is the position velocity diagram. Note that in Figure 12 the Northern part of the nebula, in projection, is clearly bent to the right, indicating blue shift with respect to the bulk of the gas. As described by Westmoquette et al. (2010), when a gas cloud hits a molecular cloud, it flows around it and we see only the components that are facing towards us (blueshift), given that the components that go behind the cloud are screened by the cloud itself. This process may be happening in the Northeastern filament, with gas clouds coming from the Southwest and hitting a large molecular cloud detected by several previous works (e.g. Rubio et al. 1988 and references therein). This process which here appears to happen in a scale of 25 pc or larger scales has also been suggested by Westmoquette et al. (2010) to occur around the Eastern pillar of NGC 6357 in a much a smaller scale.

6 SUMMARY AND CONCLUSIONS

We present the first results obtained with a Fabry-Perot mounted inside SAM, a ground-layer adaptive optics instrument using laser, on SOAR. The data cubes had a spectral resolution of $R \approx 11200$ at $H\alpha$ and a FWHM of ≈ 0.6 arcsec. This configuration provides a unique tool to study the kinematics of a variety of astronomical sources, such as normal and interacting galaxies, merging objects and Galactic objects such as HH objects, planetary nebulae, and Giant HII regions, with good spatial and spectral resolution.

In order to highlight the capabilities of the instrument, we observed the region of 30 Doradus, for which there are previously published kinematic data. We show an overall kinematic description of the central part of the 30 Doradus nebula in the LMC. The current configuration allows us to obtain kinematic information on scales of 0.15 pc, which can be improved under better seeing conditions.

Our main conclusions on the study of 30 Dor are given hereafter:

Comparing our Fabry-Perot data with previously taken VLT/FLAMES observations, we find good overall agreement in the regions of overlap, but the SAM-FP data cubes have a filling factor 360 times higher than the comparison data cubes.

The Fabry-Perot dataset has great advantages over other multi-fiber or long-slit data in the search for bubbles in nebulae in general and in 30 Dor in particular, given its much improved spatial coverage. Analysis of the Fabry-Perot data reveal a new bubble at a projected distance of 22" South of R136 with an expansion velocity of 29.1 km s^{-1} .

The Eastern filamentary loop of 30 Dor is redshifted by $\sim 37 \pm 13 \text{ km s}^{-1}$ with respect to the Northeastern filament indicating that these complexes are kinematically independent.

A velocity gradient in the Northeastern filament increases to more negative velocities running from West to East. This suggests the presence of a gas flowing around the molecular clouds, where we only see the component facing towards us. A similar mechanism was invoked in smaller scales around the Eastern pillar of NGC 6357 (Westmoquette et al. 2010)

Small high-velocity clouds are seen inside the cavity known as "Christmas tree". These are also the same kinds of phenomena reported by Redman et al. (2003), where the shell is fragmented by perturbations (such as small molecular clouds) in the medium.

In a future paper we will focus on the analysis of the whole data cube and we will specifically study the ionized gas structure around the massive stars, the relationship between their spectral types, evolutionary stage and the kinematics of $H\alpha$ profiles associated to them. The aim is to identify a number of pristine HII regions and small bubbles around massive stars and to evaluate the evolutionary scenario of the bubbles. In this context, we will attempt to describe the elusive kinematics of the small bubbles in the caldera of a giant HII region (only possible with the data taken in this work). Finally, this new instrument opens the possibility of exploring the synergy between HST and FP data given that the wealth of details seen in HST images of nearby giant HII regions can now be matched by similar quality kinematic data taken from the ground, with SAM-FP with laser correction.

7 ACKNOWLEDGMENTS

We warmly thank Marco Bonatti for writing the control software for scanning the Fabry-Perot inside SAM. We thank Brian Chinn for designing the mechanical mount for including the Fabry-Perot in

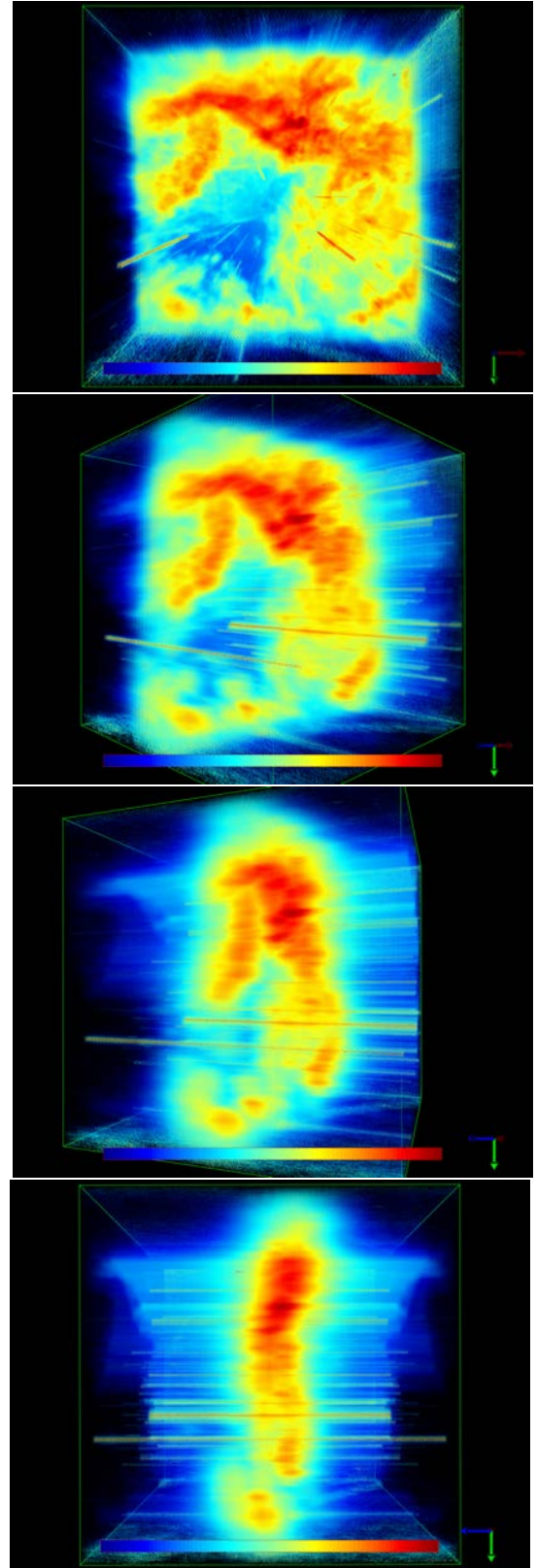


Figure 12. 3D view of the $H\alpha$ Fabry-Perot data cube of the central part of 30 Doradus with rotation around the declination axis. Top, frontal view of 30 Doradus; second from top to bottom: 45-degree view; third from top to bottom: 70-degree view; bottom: 90-degree view. Regions of highest to lowest intensity are shown in red, yellow and blue colors. Straight lines are the stars of the field. This Figure was prepared with the software GLnemo2 for better visualization purpose.

SAM. We thank Drs Warrick Couch, Matthew Colless and Sylvain Veilleux for kindly loaning us the Fabry-Perot instruments used for this work. We thank Andrei Tokovinin for extensive help with the observing runs and for very useful comments on the manuscript. We are grateful to Tiago Ribeiro for taking the image of 30 Doradus used in Fig. 2 with the T80-South telescope and to the T80-South team for allowing us to use the image in this paper. We greatly appreciated the help by Luciano Fraga, who agreed to exchange one of his nights with ours, allowing tests and science observations to be done with SAM-FP. We thank Mohamed Belhadi and Amandine Caillat from LAM for measuring the passbands of the interference filters in several configurations. We are greatly in debt to Keith Taylor, Rene Laporte and INPE, for continuous support over the last many years to the BTFI and SAM-FP teams. ST-F and RB acknowledge financial support of the Dirección de Investigación of the Universidad de La Serena and FONDECYT Project 1140076. CMdO and DA thank FAPESP and CNPq for financial support through grants 2009/54202-8 and 2014/07586-2. CMdO and PA acknowledge support of the USP-Cofecub international collaboration program, which made this project possible. Based on observations obtained at the Southern Astrophysical Research (SOAR) telescope, which is a joint project of the Ministerio da Ciência, Tecnologia, e Inovação (MCTI) da República Federativa do Brasil, the U.S.A. National Optical Astronomy Observatory (NOAO), the University of North Carolina at Chapel Hill (UNC), and Michigan State University (MSU).

REFERENCES

- Atherton, P.D., Taylor, K., David Pike, C. et al. 1982, MNRAS, 201, 661
 Amram, P., Marcellin, M., Boulesteix, J., Le Coarer, E. 1989, A&AS, 81, 59
 Barbá, R. H., Rubio, M., Roth, M. R. and García, J. 2003, AJ, 125, 1940
 Bland, J., Taylor, K., Atherton, P.D. 1987, MNRAS, 228, 595
 Chu, Y. H., Kennicutt, Jr. R. C. 1994, ApJ, 425, 720
 Crowther, P. et al. 2010, MNRAS, 408, 731
 De Marchi, G., Panagia, N. 2014, MNRAS, 445, 93
 Dimeo, R., PAN User Guide, available online at <ftp://ftp.ncnr.nist.gov/pub/staff/dimeo/pandoc.pdf>
 Fraga, L., Kunder, A., & Tokovinin, A. 2013, AJ, 145, 165
 Hénon, M. 1961, Ann.d'Ap., 24, 369
 Melnick et al. 1999, MNRAS, 302, 677
 Mendes de Oliveira, C., Taylor, K., Quint, B., et al. 2013, PASP, 125, 396
 Nazé, Y., Chu, Y.-H., Points, S. D., Danforth, C. W., Rosado, M. and Chen, C.-H. R. 2001, AJ, 122, 921
 Pellegrini, E.W., Baldwin, J. A. Ferland, G. J. 2010, ApJS, 191, 160
 Redman, M.P., Al-Mostafa, Z. A., Meaburn, J., Bryce, M. 2003, MNRAS, 344, 741
 Tokovinin, A., Tighe, R., Schurter, P., et al. 2008, Proc. SPIE, 7015, article id. 70154C
 Tokovinin, A., Tighe, R., Schurter, P., et al. 2010, Proc. SPIE, 7736, article id. 77363L
 Tokovinin, A., Tighe, R., Schurter, P., et al. 2012, Proc. SPIE, 8447, article id. 84474H
 Torres-Flores, S., Barbá, R., Maíz Apellániz, J., Rubio, M., Bosch, G., et al. 2013, A&A, 550, A60
 van der Walt, S. and Colbert, S.C. and Varoquaux, G., 2011, Computing in Science Engineering, vol 13, pp. 22-30
 Walborn, Barbá & Sewilo 2013, AJ, 145, 98
 Walborn, N. R. and Blades, J. C. 1997, 112, 457
 Walborn, N. R., Sana, H., Simón-Díaz, S. et al. 2014, A&A, 564, A40
 Westmoquette, M.S., Slavin, J.D., Smith, L.J., Gallagher, J.S., III 2010, MNRAS, 402, 152
 Astropy Collaboration, Robitaille, T. P., Tollerud, E. J., et al. 2013, A&A, 558, A33

APPENDIX A: WHAT IS NEEDED FOR CARRYING OUT FABRY-PEROT OBSERVATIONS

This appendix is written as a recipe. First we describe how to select the interference filter and the calibration lamp. Then we give the list of parameters that need to be provided/computed to observe with SAM-FP. Finally some recommendations on how to perform the observations are given. Section 2.2 of the main text and Appendix B explain why these steps should be followed.

A1 How to choose the right calibration lamp?

The calibration lamp must contain at least one emission line passing through an available interference filter. To minimize the phase-shift effect, the calibration interference filter should ideally be the target interference filter (defined here as the interference filter suitable for the observation of the on-sky target). However, often no narrow emission lines are available within the target interference filter, so the observer should select a calibration-lamp narrow emission line as close as possible to the observed emission line ($H\alpha$ in our case, redshifted due to the velocity of the target). Around $H\alpha$ or $N[II]$, the 6598.99 Å Neon emission line is suitable for nearby objects and the CTIO filter [6600/20] Å can then be used. Further explanations are given in Section B1.

A2 How to choose the right interference filter?

The Fabry-Perot may cover the spectral range 4000-7500 Å. Within this spectral range, the observer should choose the spectral range of interest that will be selected by the target interference filter. The FWHM of the target interference filter should be larger than the FSR. The FSR (formula 2) depends on the wavelength and on the interference order and it is typically 11 Å for the high resolution Fabry Perot described in this paper. Thus the target interference filter must have a FWHM between 12 and 25 Å. The right interference filters have to be chosen for both the calibration and object observations. Further explanations are given in section B2.

Besides the filters available in the CTIO filter list, the following BTFI filters are available for use in SAM with the high-resolution Fabry Perot: BTFI 5020.9/16.5, 6569.2/18.6, 6578.8/19.9, 6600.5/19.3 and 6745.5/38.6. These are 3×3 inch² filters. The BTFI 6569.2 filter was not available at the time the 30 Dor observations were taken. Since this filter has only been obtained at the end of 2015, we had to use a smaller 2×2 inch² filter from the CTIO list with approximately the same central wavelength for the 30 Dor observations.

The filter should be mounted in the filter wheel of the instrument during day time.

A3 Which input parameters are needed for SAM-FP?

A3.1 How to compute the optimal number of steps?

The computation of the optimal number of steps n needed to scan a FSR is described in this section. To satisfy the Nyquist-Shannon's sampling criteria, Δe_A must be sampled at least on two channels. To minimize the number of channels to scan, the Airy function is scanned with approximately two channels only, thus the number of channels n (corresponding to n times the plate separation e_n) needed to scan a FSR is $n = (2 \times F)$. Given that F is a float number and n is an integer, then $n = (2 \times F) + 1$. For instance the ICOS ET-65 etalon used for this work has a finesse $F \approx 18.5$, thus $n = 38$.

The observer is nevertheless free to choose another number of steps n in order to undersample or oversample the scanning sequence but of course it will not change the resolution R_λ . This is indeed what we did, in the case of 30Dor observations, we gently oversampled the scanning of finesse by 10% leading to $n = 40$ scanning channels and to a scanning step of 12.8 km s^{-1} . The determination of the FSR and of the Finesse are given in sections B3.2 and B3.3 respectively.

A3.2 How to choose the scanning wavelength ?

The scanning wavelength for the object must correspond to its mean radial velocity. The scanning wavelength for the calibration must be the wavelength of the calibration line, in our case Ne 6598.95 Å.

A3.3 Which range to scan?

The observer may chose to scan a fraction of the FSR, exactly the FSR or more than one FSR. The first option is not recommended for the p=609 high-resolution Fabry-Perot because the whole FoV will not be covered by the FSR. The third option could be selected if the observer needs to check the FSR during the reduction procedure. To optimize the observing time we recommend to scan exactly one FSR. Further technical details on the way to best define the scanning sequence is provided in section B3.4.

A3.4 How to choose the observing time ?

The observer has to determine the observing time per individual channel. This time is a compromise between a reasonable time for the total time spent on target at a given stable atmospheric condition and the optimization of the use of the detector (given its read noise characteristics). Cosmic ray hits also impose an upper limit to the exposure time per channel (to a maximum of about 5 minutes). In practice, the exposure per channel should not be longer than 2 minutes, given that, for instance, in a sequence of 40 channels, this leads to 80 minutes for the total cycle (plus overhead), which is already a long time during which the atmospheric conditions may have changed (airmass, transparency and seeing). A shorter exposure time per channel is not advisable for low-surface brightness objects, given the readout noise of the CCD (see Table 1). In case the observer wants to increase the signal-to-noise ratio of the observation, several cycles should be repeated. Short exposure times per channel (say 10-30 seconds) are suitable for high surface brightness sources (e.g. bright planetary nebulae, bright HII regions, quasars).

A3.5 How to choose the pixel binning?

As explained in 2.2.2, a binned pixel of size 0.18" (4x4) allows a good sampling of the best seeing (even with GLAO correction) and considerably increases the SNR per unit surface.

A4 Standard observing procedures

A4.1 About wavelength calibrations

Once the scanning sequence is defined, the observer can use it for the wavelength calibration. We recommend the user to take lamp calibration frames during the afternoon to check the Fabry-Perot set-up and the scanning procedure (in this case we remind the user that the scanning wavelength must be zero). As explained in section 2.2.2, we also recommend that the observers do wavelength

calibration before or after the target exposure with the telescope in the same position to match as much as possible the conditions of the observations.

A4.2 About subtraction of the night sky-line emission

If the target does not fill the whole FoV of the detector, the night sky line could be safely subtracted during the reduction procedure. If the target does fill the whole FoV, two cases may be envisaged. Firstly, if the spectral density is rather low (i.e. the average wavelength range of the target emission line per pixel is less than about one third of the FSR), the night sky line could be identified using medians during the reduction procedure. Secondly, if the spectral density is high, it is recommended to measure the sky from a new pointed observation on a target-free location, just beside the target. As the sky is expected to not have spatial structure within the SAMI FoV, a short exposure should be enough (typically one tenth of the exposure time used for the target).

A4.3 About flux calibrations and flat fields

The flux calibrations should be done using standard procedures like any other instrument, i.e. by observing calibration standards. We nevertheless recommend to use spatially extended calibrated emission line sources line planetary nebula. A scanning sequence with the same parameters used for the target observations must be used (with the important difference that the scanning wavelength must be the wavelength of the calibration source, i.e., in the case of a planetary nebulae it should correspond to the radial velocity of the planetary nebula). Flat fields should be taken to correct the spectrum from pixel to pixel efficiency variations and the effect of the interference filter transmission curves. The Fabry-Perot should be out of the FoV during the procedure of obtaining flat fields (so no scanning is necessary).

APPENDIX B: WHAT IS NEEDED FOR UNDERSTANDING FABRY-PEROT OBSERVATIONS

To complement the main text and Appendix A, this appendix gives the relevant explanations to understand Fabry-Perot observations.

B1 Wavelength calibrations and phase-shift effect

Observing a few reference calibration cubes for subsequent checking of the Fabry Perot parameters and wavelength calibration of the science data cubes must be done before taking on-sky observations. This is usually done in the afternoon of the first night of observations. As described in Appendix A1, one must select an arc line (from a calibration lamp of the SOAR calibration unit) which has a wavelength which is similar to that of the emission-line to be observed. In classical books, it is stated that the transmission curve of a Fabry-Perot is not a function of the wavelength within a given spectral band. However, in practice, the reflectivity of the coatings deposited onto the inner side of the two Fabry-Perot plates do depend on the wavelength. Each reflection, due to each dielectric coating, induces a phase-shift $\psi(\lambda)$ depending on λ in the range $[0, 2\pi]$ and relation (1) becomes:

$$p = \frac{2ne \cos \theta}{\lambda} - \frac{2\psi(\lambda)}{2\pi} \quad (\text{B1})$$

What happens is that the coatings, which consist of the superposition of multiple thin dielectric layers (typically 0.1-1 μm each), alternating transparent dielectric material with low refractive index (typically $n \approx 1.5$) and high refractive index (typically $n \approx 2.5$), are meant to provide a uniform electric field penetration depth within a given spectral range but this aimed uniformity is never perfectly achieved. This then induces a phase-shift that should be accounted for. If we observe $\text{H}\alpha$ close to its rest wavelength (which is the case for galactic HII regions, inter-arm regions, planetary nebulae, SNR, or galaxies belonging to the Local Group for which systemic heliocentric radial velocities are low or even negative), the ideal situation would be to use a Hydrogen lamp to select the $\text{H}\alpha$ emission as the calibration line, so that calibration and observed wavelengths were very similar. However, given that the $\text{H}\alpha$ emission line is intrinsically rather broad, it is better to choose a narrower emission line close to $\text{H}\alpha$ 6562.78 Å redshifted to the velocity of the target. As explained previously, we usually use Ne 6598.95 Å as the reference line, for its intrinsic narrower shape and higher intensity, allowing accurate measurements. For redshifted objects like nearby galaxies, this Ne line is very well suited because it is close to the observed redshifted $\text{H}\alpha$ line ($\lambda=6598.95$ Å corresponds to the wavelength of $\text{H}\alpha$ for an object with a radial velocity of $\sim 1650 \text{ km s}^{-1}$). We note that, in order to take observations with a low-interference order Fabry-Perot, usually called a tunable filter, several calibrations are needed to cover the broad FSR but for a high-order Fabry-Perot, which has a small FSR, one spectral line is enough.

B2 Interference filters

B2.1 Suitable interference filters

In order to complement the basic Fabry-Perot formula (1, 2, 3 and 4) given in section 2.2.1, we must introduce the Airy function. A Fabry-Perot provides a periodic signal. The transmitted intensity I_t is described by the Airy function:

$$I_t = \frac{I_t^{\max}}{1 + \frac{4}{\pi^2} F^2 \sin^2(ne \cos i)} \quad (\text{B2})$$

where I_t^{\max} is the maximum transmitted intensity, F the Finesse, n the refractive index, i the beam inclination and e the gap between the etalons.

Considering formula B2, and as mentioned in Section 2.2.1, in order to select one or few orders, an interference filter must be chosen. The central wavelength of the interference filter should correspond approximately to the mean velocity of the source. Depending on the science case, the observer can choose a filter allowing to select more than one FSR and make *a posteriori* correction but, in practice, more than three FSR might become very confusing, especially for galactic sources. In addition, all the continuum emission selected by the interference filter passes through the Fabry-Perot and it is modulated by the transmission curve of the filter. Thus, in order to increase the contrast of the Fabry-Perot (i.e. the monochromatic detection power), the interference filter should be as narrow as possible to minimize the continuum emission passing through the Fabry-Perot given that the photon noise \sqrt{N} of a continuum emission will limit the monochromatic detection. Moreover, in order to lower the continuum modulation, the passband of the filter should be as square as possible.

Table B1. Wavelength blue-shift of interference filter transmission curves

inclination ($^\circ$)	blue-shift (Å)	
	H β 4861 (Å)	H α 6563 (Å)
0	0	0
1	-0.2	-0.3
2	-1.0	-1.3
3	-2.1	-3.0
4	-3.8	-5.2
5	-6.0	-8.1
6	-8.5	-11.6

B2.2 More on interference filters

The observer has to take into account that the filter passband is blue-shifted when (i) the incidence of the incoming light is not normal to the filter, (ii) the temperature drops and (iii) the filter ages. In addition, the filter peak transmission is reduced and the FWHM is enlarged for (i) and (ii).

For small angles, the peak wavelength of the interference filter is a function of the beam aperture, temperature and time and it can be described by:

$$\lambda_c \simeq \lambda_o \sqrt{1 - \left(\frac{n_o}{n_f}\right)^2 \sin^2(\theta + i) - \alpha(\lambda_o)(T_o - T) - A(t)} \quad (\text{B3})$$

where λ_c is the corrected central wavelength of the interference filter and λ_o the central wavelength at normal incidence; $n_o \approx 1$ and n_f are the air refractive index and filter effective refractive index respectively; θ and i are the beam aperture (the focal ratio at SAM focus is $f/16.63$ providing $\theta \approx 1.7^\circ$) and filter inclination respectively; T and T_o are the ambient and reference temperature respectively, $\alpha(\lambda_o)$ a coefficient that slightly depends on λ and finally $A(t)$ a coefficient that depends on the aging of the filter and must be measured over a long period.

The three cases i, ii and iii mentioned above will be discussed in the following.

(i) Narrowband interference filters are thin and solid Fabry-Perot interferometers usually operating in first order. The air gap is replaced by a thin layer of dielectric material (also called cavity) designed with an optical thickness optimized for the desirable transmission wavelength. Multiple-cavity filters provide steeper band slopes (thus square passbands) by alternating layers of high-index material (typically Ta_2O_5 , $n_H \approx 2.13$) and low-index material (typically SiO_2 , $n_L \approx 1.46$). The effective refractive index of the filter is $n_f \simeq \sqrt{n_H n_L} \approx 1.76$.

We have measured in the lab at the Laboratoire d'Astrophysique de Marseille the central wavelength blue-shift when inclining to a small angle $0^\circ < i < 6^\circ$ a set of ~ 20 interference filters. In order to experimentally measure n_f , but especially to determine an empirical and operational relation, we fit the first term of the equation (B3) to the data. We find $n_f = 1.72^{+0.35}_{-0.22}$. The scatter is quite high from one filter to another despite the fact that the process of fabrication of the filters is the same for the two subsamples of ~ 10 filters. For convenience, in table B1, we tabulate values computed for the shift using the previous formula, for $n_f = 1.72$.

In practice, the filter could be inclined to voluntarily blue-shift the transmission curve, but the inclination should be small (typically lower than a couple of degrees) because it enlarges the passband and decreases the transmission. Moreover the shifts in wavelength do not increase linearly, becoming quite large beyond angles of

6 degrees. The SAMI filter wheel does not presently allow us to incline the filters.

In formula B3, the angle θ represents the aperture beam of the focal plane in which the filters are usually located. Usually Fabry-Perots are located in focal reducers to lower the focal ratio and increase the FoV. The aperture θ is furthermore a telescope or focal reducer-dependent parameter. SAMI is not a focal reducer, the focal ratio in the filter plane is the one of the telescope (f/16.63).

(ii) The ambient and reference temperature are usually different. Manufacturers typically provide a reference temperature $T_o=20^\circ\text{C}$ but the temperature during the observation is usually lower. To measure the temperature dependence, we used data provided by the company Melles Griot, Optics & Photonics Company. From their data we obtained:

$$\alpha(H_\alpha \text{ } 6563\text{\AA}) = \frac{\Delta\lambda}{\Delta T} = 0.24 \pm 0.01 \text{ \AA } K^{-1}$$

Other manufacturers provide lower values of α , ranging from 0.15 to 0.19 $\text{\AA } K^{-1}$ in the R-band. Using the Melles Griot data, within the optical range, we computed a weak dependence of α with λ , $\alpha = 0.175 \frac{\lambda}{\lambda_{H\alpha}} + 0.063$, providing for instance $\alpha(H_\beta \text{ } 4861\text{\AA}) = 0.19 \pm 0.01 \text{ \AA } K^{-1}$.

(iii) The aging effect on the wavelength blueshift is very difficult to generalize because it affects differently each filter, even for a set of filters having the same age and built by the same company. It depends on the use and storage conditions. The filters measured in this experiment have, however, the same "history" and we measure $A(t \approx 15 \text{ years}) \approx 3 \pm 3 \text{ \AA}$. Some filters even display a red-shifted passband but the measurements done more than 15 years later might be realised with different setups.

In addition, transmission curves of old filters may completely collapse and their FWHM dramatically increase. We measured peak transmission of 15 year-old filters down to 24-40% and as broad as 31-45 \AA (for filter showing initially a peak transmission of 70% and FWHM=20-24 \AA respectively). The 15 year-old set of filters we measured show a mean transmission of $54 \pm 16\%$ and a mean FWHM of $24 \pm 9.7 \text{ \AA}$ to be compared with their initial mean transmission of $71 \pm 2\%$ and initial mean FWHM of $17.6 \pm 4.2 \text{ \AA}$ (the initial FWHM scatter only reflects the fact that their initial widths ranged from 12 to 24 \AA , but the increase on the scatter is significant). Here again, even if their process of fabrication, conditions of use and storage are similar, the scatter in peak transmissions and widths is very high, meaning that some filters still exhibit good transmission curve even if they are older while others do not and they are, in practice, not useful any longer. The conclusion is that filters must be regularly measured.

B3 Determining FP parameters

B3.1 Determining the interference order p

Formula (1) gives the interference order p . Although a rough number for the interference order is given by the manufacturer of the Fabry-Perot, it is also possible to measure it more accurately taking into account that the distance between the plates may vary slightly. This is, however, quite tricky, given that two different methods are needed to measure the integer part of p , $p_o=\text{int}(p)$, and its fractional residual, $\epsilon=p-\text{int}(p_o)$. However, for our purposes, the value of p_o is the most important, which simplifies the computation. This

is achieved using two lines having two different wavelengths using the classical method of coincidences. Indeed, by determining where the interference rings coming from the two different wavelengths coincide one can find p_o . ϵ is computed by measuring the radius distribution of the parabolic rings.

B3.2 Measuring the FSR

Formulas 2 and 3 give the FSR in wavelength and as a function of the Fabry Perot plate separation, respectively. In this section we will detail how to compute and measure it. It is important to measure the FSR before the observing run (from calibration cubes) in order to minimize the observing time spent on-object without losing any information. Indeed our goal is to do a scanning cycle on-object that corresponds exactly to one FSR or it is just slightly larger. If the scanning sequence covers less than one FSR, some areas of the field-of-view will not be observed and some wavelengths will be missing as well. If the scanning sequence covers $x \times \text{FSR}$ (with $x > 1$), some $(x - 1)$ interferograms are redundant and are useless because the new incomplete cycle does not cover a whole FSR. The FSR should be determined once during the setup of the instrument, measured at the calibration wavelength λ_c . If λ_c is close to the observed wavelength λ_o , the phase shift is negligible and, using relations (1) and (3), it is straightforward to compute the FSR at λ_o from the FSR computed at λ_c . In practice, the determination of the FSR is done by scanning a gap slightly larger than the expected Δe_{FSR} in order to get more than two maxima of the cyclic Airy function.

If e_m is the mean distance between the plates around which the plates could be adjusted, and Δe_M the maximum gap physically reachable between the plates (limited by the course of the piezoelectric actuators), the distance between the plates of the interferometer varies in the range $\sim [(e_m - \Delta e_M)/2, (e_m + \Delta e_M)/2]$. Recall that in section 2.1 it was mentioned that the CS100 contains two channels, X and Y , to control the parallelism between the Fabry-Perot plates, and a Z channel to control the spacing. When used with the ICOS ET-65, the Z offset between the plates has a full dynamic range of 12-bit binary number. Thus, the maximum number of Binary Control Values (BCV) is $\Delta Z_M = 2^{12} = 4096$, spanned within the range $[-Z_m, Z_m - 1 = +2047]$. ΔZ_M corresponds to approximately 2 μm of plate separation adjustment. For the CS100 controller that drives the ICOS ET-65 etalon, the range of $\Delta e_M/2 \approx \pm 1 \mu\text{m}$ around e_m can be reached using a $\pm 10\text{V}$ differential input, with a non-linearity of the scan of $\pm 1\%$ and with a response time of 1 ms at a frequency response of 160 Hz (3dB)¹². The smallest increment of plate separation adjustment δe is thus

$$\delta e = \frac{\Delta e_M}{\Delta Z_M} \quad (\text{B4})$$

Furthermore, the number of BCV needed to scan the full FSR, ΔZ_{FSR} , is linked to the corresponding increment of plate separation to scan the FSR, Δe_{FSR} , and to the smallest increment of plate separation, δe , by:

$$\delta e = \frac{\Delta e_{FSR}}{\Delta Z_{FSR}} \quad (\text{B5})$$

δe is the physical expansion of the piezo-stacks for 1 BCV step applied to the etalon.

¹² from ICOS, CS100 Controller and ET Series II User's Guide.

The exact value of the gap between the plates e and δe are not known with high accuracy. We need to determine them using e.g. the calibration line λ_c . In order to switch from the expression of the FSR in terms of plate separation to the relation of the FSR as a function of the wavelength, we use the term on the right of equation (3) to define the “Fabry-Perot scanning constant” Q . When the two plates of the Fabry-Perot device are parallel, we can compute Δe_{FSR} at the center of the rings ($\theta = 0$), thus with $n = 1$, relations (3) and (B5) lead to:

$$Q = 2 \delta e = \frac{\lambda}{\Delta Z_{FSR}} \quad (\text{B6})$$

The “Fabry-Perot scanning constant” Q is equal to twice the smallest increment of plate separation δe , conventionally given in units of Å. In the present case, for the ICOS ET-65 Fabry-Perot, relation (B4) provides a rough value $Q_{rough} \simeq 2 \times 1 \mu\text{m}/2048 \simeq 9.8 \text{Å}$. The physical expansion of the piezo-stacks for 1 BCV step δe (thus Q) depends on the electronics of the controller that commands and controls the piezoelectric. In addition, it varies slightly with temperature, pressure and humidity and should be measured with accuracy. Several methods could be used, the simplest is to start from a given interferogram (ring image) and increase the BCV with very small steps, i.e. high sampling, to cover more (e.g. 10-20% more) than the expected FSR. A highly oversampled calibration cube, with spectral coverage of more than one FSR, should be obtained in day time, ahead of the first night of observation, for this purpose and for computing the finesse. The image for which the initial pattern is observed a second time indicates that a FSR has been scanned and $\Delta Z = \Delta Z_{FSR}$. For instance, applying this procedure to the high resolution Fabry-Perot with $p \simeq 609$ at Ne 6598.95 Å, we measure $\Delta Z_{FSR} \simeq 705 \text{BCV}$ (which is $\sim 17\%$ of the maximum range ΔZ_M). This now allows an accurate determination of Q using relation (B6): $Q_{acc} = 9.360 \pm 0.003 \text{Å}$ at 6598.95 Å.

B3.3 Measuring the Finesse

Formula (B2) provides the Airy function which depends on the Finesse F . This section explains its nature and how to measure it. On classical books on Fabry-Perot, the finesse F only depends on the reflectivity R_o of the coating and could be computed using the optical finesse which is the mirror reflectivity finesse:

$$F_o = \frac{\pi \sqrt{R_o}}{1 - R_o}. \quad (\text{B7})$$

We have already mentioned that the reflectivity varies with wavelength and in practice F also depends on many other factors, which depend on the location of the Fabry-Perot device in the optical path, as described below.

If the Fabry-Perot is placed in the focal plane, beam aperture induces a shift on the transmitted wavelength as well as broadening of the Airy function. The finesse will then be a function of the beam aperture f/d where f is the focal length and d the diameter of the mirror and is referred to as F_a , the aperture finesse. F_a increases linearly with the interference order p , i.e. with the resolution, but it does not depend on the wavelength for a given p .

On the other hand, if the Fabry-Perot is placed in the pupil plane, which is the case for SAM-FP, then the beam for a given extended source on the sky is supposedly a collimated beam that intercepts the surface of the Fabry-Perot. However, the light rays are never strictly parallel, which affects the image quality. This is

accounted for by the so called “Imaging Finesse” or F_i . In addition, due to defects on the surface of the Fabry-Perot plates, the transmitted wavelength is not exactly the same everywhere. This is accounted for by the so called “Defect Finesse” or “Surface Quality Finesse” or F_s . The effective finesse F is thus a combination of the optical finesse F_o , the imaging finesse F_i and the defect (or surface quality) finesse F_s . Assuming the finesse functions are close to Gaussians (which is obviously not the case), in a pupil plane, the nominal finesse is computed as:

$$\frac{1}{F^2} = \frac{1}{F_o^2} + \frac{1}{F_i^2} + \frac{1}{F_s^2} \quad (\text{B8})$$

F_i depends on the illumination of the Fabry-Perot and, therefore, on the input beam diameter. We can define F_i as:

$$F_i = \frac{\lambda}{2ne\Delta\theta \sin\theta} \quad (\text{B9})$$

where θ is the beam aperture and $\Delta\theta$ the image quality. Note that, for a given image quality, the imaging finesse depends on the plate separation and on the field-of-view. On the other hand, F_s depends on the defects due to surface roughness of the plate surface and coating deposit inhomogeneities, on the alignment (accuracy of the parallelism between the plates), on the stress between the plates inducing mirror curvature, on the tilt angle of the interferometer and on the electronics and mechanics (electric and mechanic stability of the positioning at a given plate separation e , electronic gain of the controller, etc); all these contribute to random position-dependent optical path length differences, that may cause unwanted phase shifts at each reflection, symmetrically blurring (broadening) the line-shape.

Luckily, in practice, the effective finesse, F can be easily measured during the setup. This is achieved by obtaining e.g. a scanning sequence at high sampling also needed for computation of the FSR (as explained above). We use the formulae:

$$F = \frac{\Delta e_{FSR}}{\Delta e_A} \quad (\text{B10})$$

where Δe_A is the FWHM of the Airy function or, more precisely, it is the increment in plate separation (in microns) necessary to cover one FWHM of the Airy function while e_{FSR} is the increment of plate separation necessary to scan the FSR.

Using relations (3) and (B10) we find:

$$\Delta e_A = \frac{e}{pF}. \quad (\text{B11})$$

The finesse can be obtained, in practice, by extracting a 1D spectrum from a calibration cube, e.g. in the center of its rings (where $\theta = 0$) and by measuring the width of an arc line (e.g. 6598.95Å). F is then obtained by dividing FSR by the width of this arc line.

We measured a finesse $F \simeq 18.48$ at the Ne 6598.95Å line. We measure $R \simeq 11260$ at the Ne 6598.95Å line, which gives $R \simeq 11200$ at H α 6562.78.

B3.4 Defining the scanning sequence

This section describes how to define the scanning sequence. Once the number of channels n is fixed and the Fabry-Perot constant Q is known, the scanning sequence could be defined for a given

wavelength. Reference wavelength calibration data cubes are taken at the calibration wavelength λ_c (e.g. using the Ne I emission line 6598.95 Å selected through a narrow interference filter ~ 19 Å) by scanning the FSR at λ_c . A BCV value close to $Z = 0$ (the middle of the plate separation adjustment) defines the zero point of the scanning sequence that corresponds to half of the FSR to scan. Using relation B6, e.g. at the calibration wavelength λ_c , the first channel to scan thus corresponds to the BCV $Z_1 = -\frac{\Delta Z_{FSR}}{2} = -\frac{\lambda_c}{2Q}$; the scanning step between two successive channels is $\frac{\Delta Z_{FSR}}{n} = \frac{\lambda_c}{nQ}$, thus channel 2 corresponds to $Z_2 = -\frac{\lambda_c}{2Q} + \frac{\lambda_c}{nQ}$, channel 3 to $Z_3 = -\frac{\lambda_c}{2Q} + \frac{2\lambda_c}{nQ}$ and the last channel is $Z_n = -\frac{\lambda_c}{2Q} + \frac{n-1}{nQ} \lambda_c$. Ideally, we should plan to not have an overlapping of two successive orders, thus channel 1 and channel $n + 1$ are identical. The first and the $n + 1^{st}$ channels match, as do also the second and the $n + 2^{nd}$ and so on. Finally, the step in BCV values between two successive channels $\frac{\Delta Z_{FSR}}{n}$ being an integer value, thus $n \times \text{nint}(\frac{\Delta Z_{FSR}}{n})$ (nint is the function nearest integer) is not exactly equal to ΔZ_{FSR} . The difference $|\Delta Z_{FSR} - n \times \text{nint}(\frac{\Delta Z_{FSR}}{n})|$ must then be homogeneously spread over all steps of the scanning sequence. This means that in the end the step between any two successive channels could be one BCV larger or smaller than the average step value. However, this is not a problem given that the FSR is, in any case, scanned with an accuracy better than one BCV (i.e. better than 0.14% for the present setup).

On-target observations are carried out using the same scanning sequence (number of channels) as for the calibration but at the wavelength of the observation λ_o , in order to cover the whole FSR. The number of BCV scanned is then not exactly the same as for the calibration. Indeed, to cover a full FSR at the wavelength of the on-target observation λ_o , a new sequence should be defined by $[-\frac{\lambda_o}{2Q}, -\frac{\lambda_o}{2Q} + \frac{\lambda_o}{nQ}, \dots, -\frac{\lambda_o}{2Q} + \frac{n-1}{nQ} \lambda_o]$. The zero point of the scanning sequence ($Z = 0$) should be common to all wavelength, i.e. the plate separation e of the Fabry-Perot should be the same regardless the wavelength because the relation $p_c \lambda_c = p_o \lambda_o$, deduced from relation (1) for each point in the FoV (for a fixed $\cos \theta$), is only valid for this plate separation e . Consequently, if $\lambda_o \leq \lambda_c$, $\Delta Z_{FSR}(\lambda_o) \leq \Delta Z_{FSR}(\lambda_c)$. Therefore, in addition to the phase shift mentioned in the beginning of this section, another reason to choose λ_c as close as possible to λ_o is to minimize the difference between the two FSR, minimizing the need for interpolation during the construction of the wavelength calibrated data cube. Nevertheless, here again, the observer is free to use other scanning sequences, if desired.

We described above and in Appendix A, all necessary steps to take data with SAM-FP. In practice, a Python program that computes all the parameters and sets up the observation sequence is available in the SAMI machine, ready for the observer to use.